NASA Technical Paper 1331

Comparison of Concurrent Strain Gage- and Pressure Transducer-Measured Flight Loads on a Lifting Reentry Vehicle and Correlation With Wind Tunnel Predictions

Ming H. Tang, Walter J. Sefic,
and Robert G. Sheldon

OCTOBER 1978

NASA

NASA Technical Paper 1331

Comparison of Concurrent Strain Gage- and Pressure Transducer-Measured Flight Loads on a Lifting Reentry Vehicle and Correlation With Wind Tunnel Predictions

Ming H. Tang, Walter J. Sefic,
and Robert G. Sheldon
Dryden Flight Research Center
Edwards, California

National Aeronautics
and Space Administration

**Scientific and Technical
Information Office**

1978

COMPARISON OF CONCURRENT STRAIN GAGE- AND PRESSURE TRANSDUCER-MEASURED FLIGHT LOADS ON A LIFTING REENTRY VEHICLE AND CORRELATION WITH WIND TUNNEL PREDICTIONS

Ming H. Tang, Walter J. Sefic, and Robert G. Sheldon
Dryden Flight Research Center

INTRODUCTION

Strain gages are extensively used to measure aircraft loads in flight. In general, strain gage measurement methods require many fewer transducers than pressure survey techniques. Therefore, strain gage methods are both simpler and less expensive to use.

Although the flight load measurements made with strain gages are generally satisfactory, few direct comparisons have been made between them and flight load pressure measurements (refs. 1 and 2). As part of the lifting reentry vehicle flight research program at the NASA Dryden Flight Research Center (refs. 3 to 7), the X-24B vehicle was redundantly instrumented with both strain gages and pressure transducers for the measurement of fin loads and control surface hinge moments. Flight tests were conducted at pressure altitudes from 6096 meters to 12,192 meters (20,000 feet to 40,000 feet), angles of attack from 4° to 18°, and Mach numbers from 0.6 to 1.3. The overall X-24B research program is described in Flight Planning and Conduct of the X-24B Research Aircraft Flight Test Program, by Johnny G. Armstrong (AFFTC-TR-76-11, Air Force Flight Test Center, Edwards Air Force Base, Calif., Dec. 1977).

The purpose of this paper is twofold: first, to compare the flight loads measured concurrently by the two independent systems; and second, to compare the flight fin load and control surface hinge-moment data with wind tunnel predictions.

SYMBOLS AND ABBREVIATIONS

Physical quantities in this report are given in the International System of Units (SI) and parenthetically in U.S. Customary Units. Measurements were taken in Customary Units. Factors relating the two systems are given in reference 8.

B	left fin bending moment, m-N (in-lb)
$B.L.$	butt line, cm (in.)
b	span, m (in.)
$\bar{b}$	left fin reference span, m (in.)
C_B	left fin bending-moment coefficient, $\frac{B}{qS\bar{b}}$
C_h	control surface hinge-moment coefficient, $\frac{H}{qSc}$
C_p	left fin pressure coefficient, $\frac{p_L - p_\infty}{q}$
C_T	left fin torsion coefficient, $\frac{T}{qS\bar{c}}$
C_Y	left fin normal-force coefficient, $\frac{N}{qS}$
c	average chord, m (in.)
$\bar{c}$	left fin mean aerodynamic chord, m (in.)
H	hinge moment, m-N (in-lb)
M	free-stream Mach number
N	left fin normal force, N (lb)
p_∞	free-stream pressure, N/m^2 (lb/ft^2)
p_L	local pressure, N/m^2 (lb/ft^2)
q	free-stream dynamic pressure, N/m^2 (lb/ft^2)
S	surface area, m^2 (ft^2)
T	left fin torsion, m-N (in-lb)
V	relative wind velocity, m/sec (ft/sec)
WL	water line, cm (in.)

X, Y, Z	vehicle reference axes
α	vehicle angle of attack, deg
β	vehicle angle of sideslip, deg
δ	control surface deflection, deg

Subscripts:

a	aileron
ab	aileron bias
l	lower flap
r	rudder
rb	rudder bias
rl	lower rudder
ru	upper rudder
u	upper flap
ub	upper flap bias

FLIGHT TEST VEHICLE

The X-24B lifting reentry vehicle (fig. 1) has a highly swept delta planform with three vertical fins and a boattailed afterbody. Combinations of the four chambers of the XLR11 rocket engine were used for powered flight. Because of the amount of propellant carried on board, the vehicle was limited to a maximum Mach number of approximately 1.76. Physical characteristics of the vehicle are given in table 1. A three-view drawing is shown in figure 2.

The control system of the X-24B vehicle consisted of 10 control surfaces and was powered by an irreversible hydraulic system. The control surface locations and sign conventions are shown in figure 3. Pitch was primarily controlled through the lower flaps, which were positioned by longitudinal movement of the center stick. When the lower flaps reached the fully closed position, pitch control was transferred to the upper flaps. The ailerons, which were positioned differentially by lateral movement of the center stick, provided roll control. Yaw control was obtained by deflection of the upper rudders through inputs to the rudder pedals.

The vehicle's performance and stability was adjusted at various Mach numbers by symmetrically deflecting (biasing) the upper flaps, upper and lower rudders, and ailerons. For the data in this report, the rudders were biased at 0°, the upper flaps at -40°, and the ailerons at 7° (fig. 4).

FLIGHT TEST PROGRAM

The X-24B vehicle was air launched from a modified B-52 airplane at an altitude of approximately 13,700 meters (45,000 feet) and a Mach number of approximately 0.7. The unpowered flights lasted approximately 4 minutes and were conducted below a Mach number of 0.7. For the powered flights, the rocket engine was fired 5 seconds after launch and was operated for approximately 130 seconds. The powered boost was followed by gliding flight. An entire flight lasted approximately 7 minutes. For both powered and glide flights, an angle of attack schedule was flown to achieve the desired flight profile and flight conditions for the planned data maneuvers.

In general, the maneuvers from which vehicle data were obtained were performed at altitudes above 6100 meters (20,000 feet) to allow the pilot enough time to prepare for the final approach and landing. The pushover-pullup maneuvers were performed in the pitch axis. Lateral-directional maneuvers consisted of aileron and rudder doublets performed in the roll and yaw axes.

The vehicle Reynolds number ranged from 10×10^6 to 80×10^6, based on the vehicle reference length of 11.43 meters (37.49 feet). Mach number ranged from subsonic to supersonic with a maximum of 1.76. The peak altitude was 22,595 meters (74,132 feet). The angle of attack ranged from 0° to 20°. The maximum flight and design limit fin loads and control surface hinge moments are presented in tables 2 and 3. The X-24B flight test program was not intended to explore limit load conditions; therefore, the measured loads were small in comparison to the limit loads. The maximum flight loads occurred on the lower flap and were 39 percent of the design limit.

WIND TUNNEL TESTS

Wind tunnel tests were performed on a 0.08-scale model of the X-24B vehicle in the Cornell Aeronautical Laboratory (now CALSPAN Corp.) 8-Foot Transonic Wind Tunnel (Transonic Wind Tunnel Tests on a .08 Scale Model of the FDL-8X Lifting Body (Pressure Test) by R. E. deKuyper, CAL No. AA-4024-W-3, July 1971). Pressure distributions determined over the model surfaces were integrated, and forces, moments, and centers of pressure were calculated.

The tests were conducted at Mach numbers from 0.60 to 1.30 and at the maximum free-stream Reynolds number obtainable at each Mach number. Reynolds number ranged from 15.00×10^6 to 9.75×10^6. Angle of attack was varied from -4° to 24° at a fixed angle of sideslip of -5°, 0°, or 5°.

INSTRUMENTATION AND CALIBRATION

Flight data were obtained by means of a nine-bit pulse code modulation (PCM) telemetry system. A ground-based computer was used to analyze the data.

Angle of attack and angle of sideslip were measured with an instrumented NACA nose boom (ref. 9). An inertial platform was used to measure pitch, roll, and yaw. Control surface positions were measured with control position transducers.

Strain Gages and Thermocouples

In total, 32 strain gage bridges were used to measure fin loads and control surface hinge moments. Twelve strain gage bridges were installed in the left fin, and two strain gage bridges were mounted on each of the 10 control surface actuator mechanisms.

The locations of the fin strain gage bridges and the thermocouples used to correct strain gage zero shifts are shown in figures 5(a) to 5(d).

The X-24B left fin was removed from the vehicle and mounted in the calibration fixture shown in figure 6. One hundred rubber-lined load pads were glued to the inboard skin of the fin and rudders, as shown in figure 7.

The load pads were whiffle treed in 17 different combinations, and tension loads were applied through a single hydraulic jack. The 17 calibration centers of pressure completely encompassed the wind tunnel-predicted center of pressure region. Figure 8 shows both the wind tunnel-predicted center of pressure region and the strain gage calibration points used on the fin to cover the X-24B flight envelope.

The control surface hinge-moment strain gage bridges were calibrated in place on the X-24B vehicle. Compression loads were applied through felt-lined load pads positioned on the control surfaces. For each of the 10 control surfaces, the strain gages were calibrated with the control surfaces in at least three positions. This was done in order to incorporate the variation in strain gage output due to control surface position in the calibration as well as the variation due to the calibration loads.

The fin and control surface strain gage outputs as a function of the calibration loads were used to derive appropriate loads equations by using the method given in reference 10. Corrections were made for the strain gage zero shifts due to temperature variations between the ground calibration and the flight tests.

Pressure Transducers

The fin and control surface pressure survey utilized 147 pressure taps installed flush on the left fin, rudders, aileron, and flaps. The locations of the fin and rudder pressure taps are shown in figure 9(a). The aileron and upper and lower flap pressure tap locations are shown in figure 9(b).

Each tap was connected to a pressure transducer with 0.318-centimeter (1/8-inch) flexible tubing. The tubing was less than 3.05 meters (10 feet) long for each tap in order to eliminate pressure lags in the data.

The pressure transducers were housed in a temperature-controlled insulated box mounted in the fuselage. All the transducers were calibrated in place on the vehicle.

ESTIMATED ERRORS

Estimates were made of the errors in each of the parameters pertinent to the presentation of the loads data. The estimates include the sensor, calibration, and data reduction errors.

Probable errors of resolution were determined for the flight strain gage shear, bending-moment, and torque equations for the left fin and the control surface hinge moments. These resolution errors are based on the PCM system error.

In addition to the resolution errors, equation standard errors were calculated for the shear, bending-moment, and torque coefficients on the left fin. To obtain the equation standard errors, the calibration data were analyzed using a method described in reference 11.

The vehicle attitude and dynamic pressure errors were obtained from reference 6.

The pressure coefficent errors were estimated using a method outlined in reference 12.

The estimated errors in the pertinent vehicle and load parameters are summarized in the following table.

α, deg	±0.65
β, deg	±0.33
q, N/m^2 (lb/ft^2)	±96 (±2)
M	±0.01
δ_a, deg	±0.50
δ_l, deg	±0.43
δ_u, deg	±0.65
δ_{rl}, deg	±0.23
δ_{ru}, deg	±0.54
C_p	±0.05
N, N (lb) —	
Probable error of resolution	±307 (±69)
Equation standard error	±507 (±114)
B, m-N (in-lb) —	
Probable error of resolution	±114 (±1005)
Equation standard error	±288 (±2546)
T, m-N (in-lb) —	
Probable error of resolution	±166 (±1470)
Equation standard error	±467 (±4137)
H, probable error of resolution, m-N (in-lb) —	
Upper rudder	±11 (±96)
Lower rudder	±16 (±137)
Aileron	±48 (±420)
Upper flap	±62 (±551)
Lower flap	±27 (±237)

RESULTS AND DISCUSSION

Left Fin Pressure Distributions

Typical flight-measured variations of left fin pressure coefficient with angle of attack and Mach number are presented in figure 10. Wind tunnel data are also presented for comparison. The flight data fairings were obtained by fitting a fifth-order equation through the flight pressure data. This fifth-order curve-fitting process was also used to integrate the pressure data to obtain the flight pressure loads presented in this report. The poorest correlation between the flight and wind tunnel pressure coefficients occurs at Mach 0.6 near the fin leading edge (fig. 10(a)).

Left Fin Normal-Force, Bending-Moment, and Torque Coefficients

The variations of left fin normal-force, bending-moment, and torque coefficients with angle of attack and Mach number are presented in figure 11. The flight data were obtained from pushover-pullup maneuvers, lateral-directional pulses, and steady-state sideslip maneuvers performed during the first 28 flights.

The agreement between flight strain gage measurements and flight pressure measurements is generally good. The largest discrepancies occur at high angles of attack and a Mach number of 0.6 (fig. 11(a)). At these conditions, the discrepancies between the strain gage- and pressure transducer-measured flight loads may be attributed to the fact that the strain gage calibration loadings matched the centers of pressure but did not match the actual flight pressure distribution. Another source of error may be the relatively sparse distribution of pressure taps near the fin leading edge, which did not permit the accurate definition of the sharp peaks apparent in the pressure survey. The flight data shown in figure 11(a) illustrate the discrepancy. At Mach 0.6 and at angles of attack greater than 12°, the pressure distribution represented by the plot in figure 10(a) for $\alpha = 15°$ results in the largest difference between the strain gage- and pressure transducer-measured fin normal-force loads.

The wind tunnel data correlate well with the flight data, except at Mach 0.6, where the wind tunnel data predict lower normal-force coefficients at low angles of attack and lower torque coefficients for the entire angle of attack range (fig. 11(a)). The wind tunnel data also predict lower torque coefficients at Mach 0.9 for the entire angle of attack range (fig. 11(b)).

The changes in left fin normal-force, bending-moment, and torque coefficients with angle of sideslip at subsonic, transonic, and supersonic Mach numbers are presented in figure 12. As with the variations of fin load coefficients with angle of attack, the poorest correlation between the flight strain gage and flight pressure data occurs at Mach 0.6 (fig. 12(a)). In general, the flight data for C_Y, C_B, and C_T as functions of angle of sideslip have slopes similar to those of the corresponding wind tunnel data.

Figure 13 summarizes the variation of normal-force, bending-moment, and torque coefficients with Mach number for an angle of attack of 10°. The flight strain gage data and flight pressure data, although scattered, compare favorably with wind tunnel values. The largest discrepancies occur at the lower Mach numbers.

Control Surface Hinge-Moment Coefficients

Upper and lower rudder.—Flight-determined variations of the left upper and lower rudder hinge-moment coefficients with angle of attack and Mach number are presented in figure 14 and compared with wind tunnel predictions. The flight strain gage and pressure data correlate well with wind tunnel predictions, except that the wind tunnel values are slightly lower for the upper rudder at Mach 0.9 (fig. 14(b)) and higher for the lower rudder at Mach 1.2 (fig. 14(c)).

The upper and lower rudder hinge-moment coefficients as functions of angle of sideslip and Mach number are presented in figure 15. In general, the correlation between the flight strain gage and flight pressure values is good. The correlation between flight-measured and wind tunnel rudder hinge-moment coefficients is good, except for the upper rudder hinge-moment coefficient at Mach 0.9, as shown in figure 15(b).

The summary plot (fig. 16) indicates the variations of upper and lower rudder hinge-moment coefficients with Mach number for an angle of attack of 10°. The strain gage and pressure data, although scattered, correlate well. For the lower rudder, the wind tunnel and flight data correlate well; for the upper rudder, the wind tunnel predicts lower values than those measured in flight.

Upper flap, lower flap, and aileron.—The pitch attitude of the vehicle is controlled with the lower flaps; hence, angle of attack and lower flap position are directly related. To isolate the effect of angle of attack and lower flap position, a linear multiple regression technique was applied to the lower flap hinge-moment data using the following equation:

$$C_{h_l} = \frac{\partial C_{h_\alpha}}{\partial \alpha}\alpha + \frac{\partial C_{h_l}}{\partial \delta_l}\delta_l$$

Figure 17 shows the variation of the lower flap hinge moment due to lower flap deflection as a function of Mach number. The dashed line represents a fairing of the regression data, and the shaded area represents the standard error of the regression. The available wind tunnel data are within the standard error of the flight data.

The regression data shown in figure 17 were used to correct the lower flap hinge-moment coefficient data to a lower flap deflection of 20°.

The variations of upper flap, lower flap, and aileron hinge-moment coefficients with angle of attack and Mach number are presented in figure 18. The lower flap

hinge-moment coefficients have been corrected to a lower flap deflection of 20°. In general, the flight strain gage data and flight pressure data correlate well.

As compared with the flight data, the wind tunnel data show lower values for the upper flap and lower flap hinge-moment coefficients at Mach 0.6 (fig. 18(a)), higher values for the lower flap hinge-moment coefficient at Mach 0.9 (fig. 18(b)), and higher values for the lower flap hinge-moment coefficient at Mach 1.2 (fig. 18(c)). The wind tunnel-predicted increase in aileron hinge-moment coefficient due to increase in angle of attack is greater than the flight-measured values throughout the Mach number range investigated (fig. 18).

Figure 19 is a summary plot of the upper flap, lower flap, and aileron hinge-moment coefficients as functions of Mach number for an angle of attack of 10°. The data show some scatter, but the correlation between flight and wind tunnel data is generally good. At the higher Mach numbers, the wind tunnel-predicted values for the lower flap hinge-moment coefficient are higher than the values obtained in flight.

CONCLUDING REMARKS

Concurrent strain gage- and pressure transducer-measured fin loads and control surface hinge moments from the X-24B flight test program were compared with wind tunnel-predicted values. Tests were conducted at subsonic, transonic, and supersonic Mach numbers.

The correlation between the concurrent strain gage and pressure transducer measurements on the fin and control surfaces was generally good. The largest discrepancy occurred for the left fin normal-force loads at Mach 0.6 and an angle of attack greater than 12°.

The correlation between the flight and wind tunnel hinge-moment measurements is in general better than the correlation between the flight and wind tunnel fin load measurements. The measurements on the fin may be improved by increasing the number of pressure taps, particularly near the fin leading edge, and by simulating the actual flight pressure distribution in calibrating the strain gage instrumentation.

Dryden Flight Research Center
National Aeronautics and Space Administration
Edwards, Calif., May 8, 1978

REFERENCES

1. Aiken, William S., Jr.; and Howard, Donald A.: A Comparison of Wing Loads Measured in Flight on a Fighter-Type Airplane by Strain-Gage and Pressure-Distribution Methods. NACA TN 1967, 1949.

2. Keener, Earl R.; and Pembo, Chris: Aerodynamic Forces on Components of the X-15 Airplane. NASA TM X-712, 1962.

3. Jenkins, Jerald M.; Tang, Ming H.; and Pearson, George P. E.: Vertical-Tail Loads and Control-Surface Hinge-Moment Measurements on the M2-F2 Lifting Body During Initial Subsonic Flight Tests. NASA TM X-1712, 1968.

4. Tang, Ming H.; and Pearson, George P. E. : Flight-Measured HL-10 Lifting Body Center Fin Loads and Control Surface Hinge Moments and Correlation With Wind-Tunnel Predictions. NASA TM X-2419, 1971.

5. Tang, Ming H.: Correlation of Flight-Test Loads With Wind-Tunnel Predicted Loads on Three Lifting Body Vehicles. Flight Test Results Pertaining to the Space Shuttlecraft. NASA TM X-2101, 1970, pp. 59-72.

6. Tang, Ming H.; and Pearson, George P. E.: Flight-Measured X-24A Lifting Body Control-Surface Hinge Moments and Correlation With Wind-Tunnel Predictions. NASA TM X-2816, 1973.

7. Tang, Ming H.: Vertical-Fin Loads and Rudder Hinge-Moment Measurements on a 1/8-Scale Model of the M2-F3 Lifting Body Vehicle at Mach Numbers From 0.50 to 1.30. NASA TM X-2286, 1971.

8. Mechtly, E. A.: The International System of Units — Physical Constants and Conversion Factors. Second Revision. NASA SP-7012, 1973.

9. Richardson, Norman R.; and Pearson, Albin O.: Wind-Tunnel Calibrations of a Combined Pitot-Static Tube, Vane-Type Flow-Direction Transmitter, and Stagnation-Temperature Element at Mach Numbers From 0.60 to 2.87. NASA TN D-122, 1959.

10. Skopinski, T. H.; Aiken, William S., Jr.; and Huston, Wilber B.: Calibration of Strain-Gage Installations in Aircraft Structures for the Measurement of Flight Loads. NACA Rept. 1178, 1954.

11. Sefic, Walter J.; and Reardon, Lawrence F.: Loads Calibration of the Airplane. NASA YF-12 Flight Loads Program, NASA TM X-3061, 1974, pp. 61-107.

12. Pyle, Jon S.: Flight-Measured Wing Surface Pressures and Loads for the X-15 Airplane at Mach Numbers From 1.2 to 6.0. NASA TN D-2602, 1965.

TABLE 1.—REFERENCE AREAS AND DIMENSIONS OF THE X-24B VEHICLE

Body —	
Reference planform area, m^2 (ft^2)	30.70 (330.50)
Reference length, m (ft)	11.43 (37.50)
Reference span, m (ft)	5.79 (19.00)
Aspect ratio (basic vehicle)	1.10
Weight, empty, N (lb)	37,809 (8500)
Center of gravity, percentage of reference length	66
Center vertical fin (airfoil stabilizer) —	
Area, m^2 (ft^2)	1.37 (14.70)
Mean aerodynamic chord, m (in.)	1.47 (57.90)
Root chord, m (in.)	1.88 (73.90)
Tip chord, m (in.)	0.96 (38.00)
Distance between root chord and mean aerodynamic center, m (in.)	0.44 (17.30)
Span, m (in.)	0.99 (38.80)
Outboard vertical fin (cambered airfoil with leading-edge droop) —	
Area, each, m^2 (ft^2)	2.41 (25.90)
Mean aerodynamic chord, m (in.)	1.92 (75.70)
Root chord, m (in.)	2.58 (101.50)
Tip chord, m (in.)	1.05 (41.50)
Distance between root chord and mean aerodynamic chord, m (in.)	0.55 (21.60)
Reference span, m (in.)	1.27 (50.10)
Upper rudder —	
Area, each, m^2 (ft^2)	0.46 (4.99)
Chord, m (in.)	0.75 (29.60)
Span, m (in.)	0.62 (24.20)
Lower rudder —	
Area, each, m^2 (ft^2)	0.62 (6.67)
Chord, m (in.)	0.75 (29.60)
Span, m (in.)	0.82 (34.20)
Aileron —	
Area, each, m^2 (ft^2)	1.37 (14.74)
Chord, m (in.)	1.21 (47.70)
Span, from *B.L.* 127 cm (50 in.), m (in.)	1.27 (49.90)
Upper flap —	
Area, each, m^2 (ft^2)	1.01 (10.82)
Chord, m (in.)	0.87 (34.10)
Span, m (in.)	1.16 (45.70)
Lower flap —	
Area, each, m^2 (ft^2)	1.30 (13.99)
Chord, m (in.)	1.14 (44.90)
Span, m (in.)	1.14 (44.90)

TABLE 2.—X-24B MAXIMUM FLIGHT AND DESIGN LIMIT LEFT FIN LOADS AND ASSOCIATED CONDITIONS

		Loads	q, N/m^2 (lb/ft^2)	M	α, deg	β, deg	δ_{rb}, deg	δ_{ub}, deg	δ_l, deg	δ_{ab}, deg
Shear force	Maximum flight	11,556 N (2,598 lb)	14,556 (304)	0.67	8.2	0	0	-20	3	7.0
	Design limit	40,033 N (9,000 lb)	23,078 (482)	1.60	5.7	-5.5	10.00	---	--	---
Bending moment	Maximum flight	6,607 m-N (58,473 in-lb)	12,832 (268)	0.53	9.1	0	-2.29	-40	23	6.8
	Design limit	21,964 m-N (194,400 in-lb)	23,078 (482)	1.60	5.7	-5.5	10.00	---	--	---
Torsion moment	Maximum flight	9,934 m-N (87,920 in-lb)	11,396 (238)	1.45	7.7	0	-0.27	-40	11	6.8
	Design limit	39,149 m-N (346,500 in-lb)	23,078 (482)	1.60	5.7	-5.5	10.00	---	--	---

TABLE 3.—X-24B MAXIMUM FLIGHT AND DESIGN LIMIT CONTROL SURFACE HINGE MOMENTS AND ASSOCIATED CONDITIONS

		Hinge moment, m-N (in-lb)	q, N/m^2 (lb/ft^2)	M	α, deg	β, deg	δ_{rb}, deg	δ_{ub}, deg	δ_l, deg	δ_{ab}, deg
Aileron	Maximum flight	2,347 (20,775)	8,235 (172)	0.50	16.4	0	-10.0	-25	1	11.0
	Design limit	12,293 (108,800)	18,530 (387)	1.00	13.3	10.0	0	-40	20	17.0
Upper rudder	Maximum flight	1,048 (9,276)	11,396 (238)	1.46	7.8	0	0	-40	11	6.8
	Design limit	2,700 (23,900)	23,078 (482)	1.60	5.7	-5.5	10.0	---	--	----
Lower rudder	Maximum flight	788 (6,977)	7,622 (159)	1.32	4.6	-1.3	4.8	-40	20	6.6
	Design limit	3,435 (30,400)	23,078 (482)	1.60	5.7	-5.5	10.0	---	--	----
Upper flap	Maximum flight	3,276 (28,998)	9,576 (200)	1.00	4.4	0	0	-40	28	6.1
	Design limit	8,869 (78,500)	23,030 (481)	1.70	4.0	0	-----	-54	--	----
Lower flap	Maximum flight	3,980 (35,229)	9,528 (199)	1.01	4.5	0	0	-40	29	6.7
	Design limit	10,169 (90,000)	22,312 (466)	1.40	12.0	0	-----	---	40	----

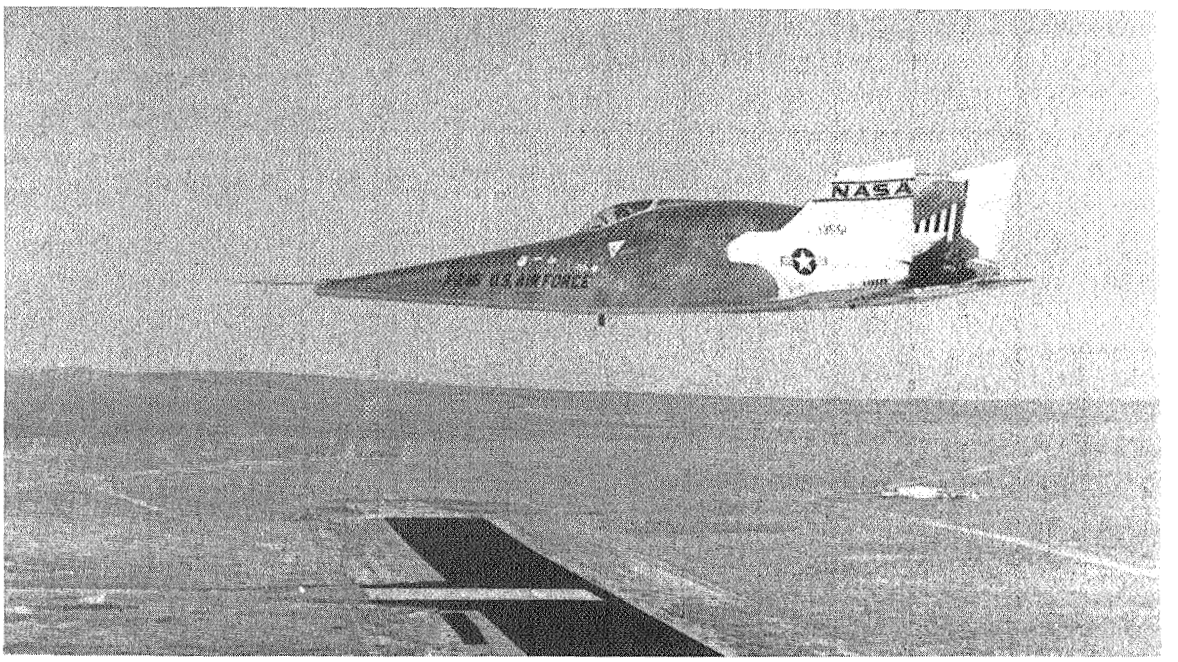

E-26620

Figure 1. X-24B test vehicle in flight.

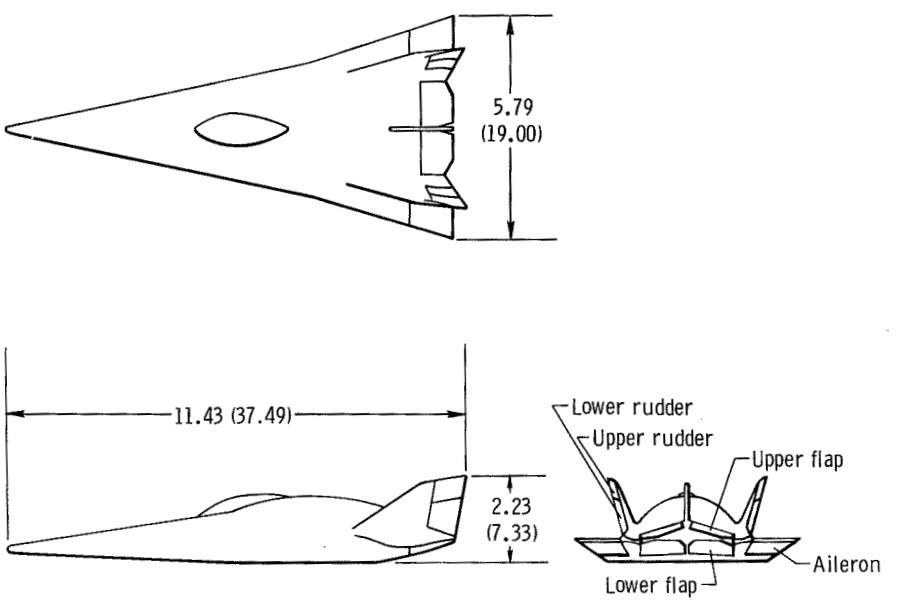

Figure 2. Three-view drawing of X-24B vehicle. Dimensions in meters (feet).

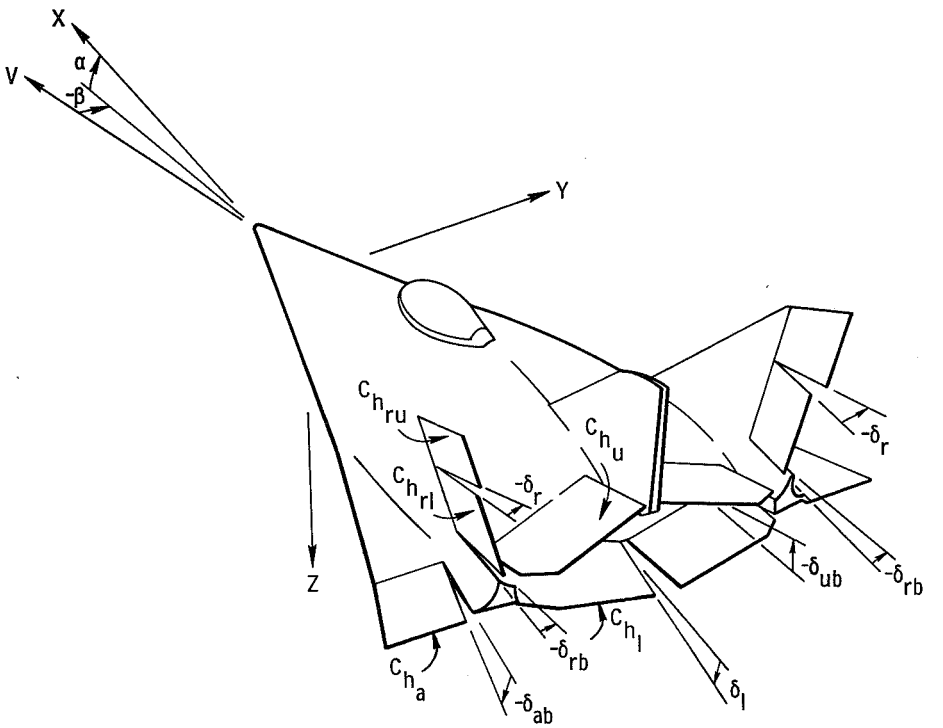

Figure 3. Sign convention for X-24B control surface hinge-moment coefficients and deflections.

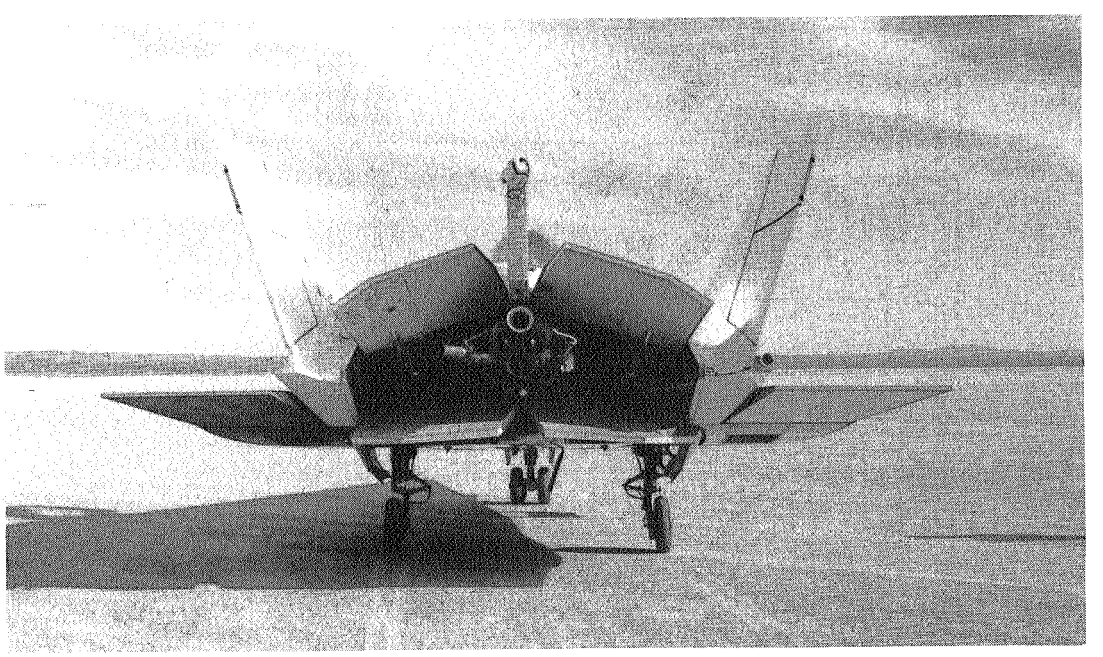

Figure 4. Rear view of X-24B flight test vehicle. $\delta_{rb} = 0°$; $\delta_{ab} = 7°$; $\delta_{ub} = -40°$; $\delta_l = 25°$.

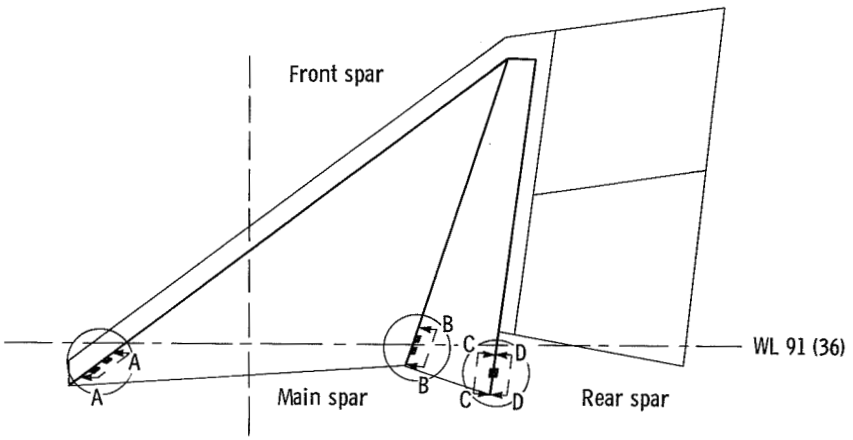

(a) Overall view.

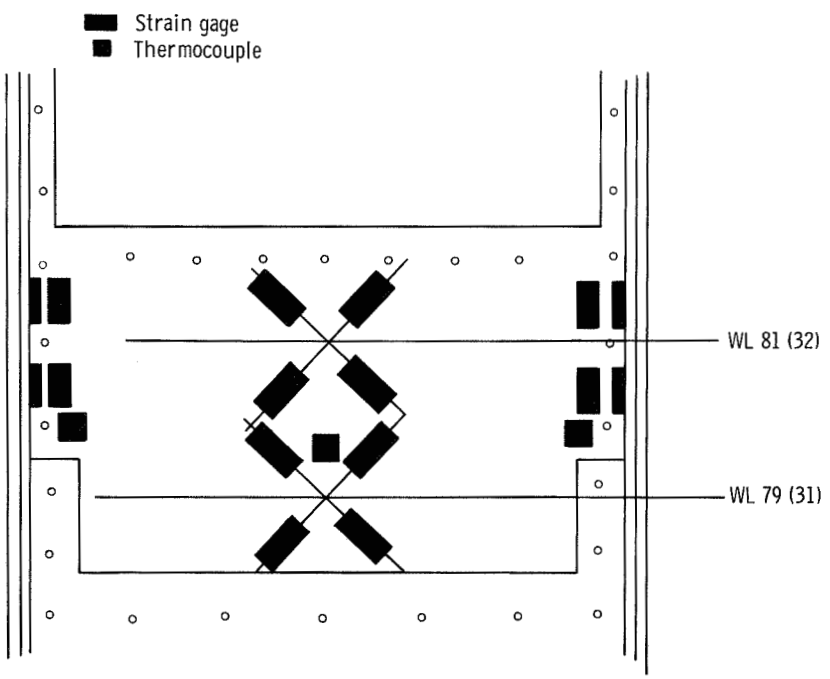

(b) Front spar, view A-A.

Figure 5. Strain gage bridge and thermocouple locations for fin and sign conventions for fin loads. Dimensions in centimeters (inches); C_Y positive in Y direction (fig. 3).

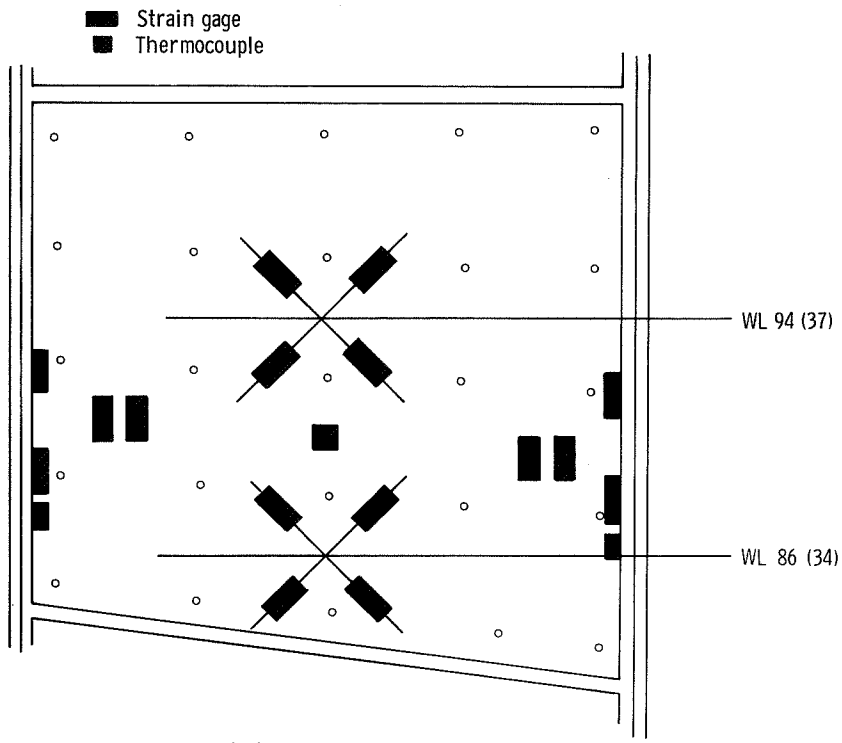

(c) Main spar, view B-B.

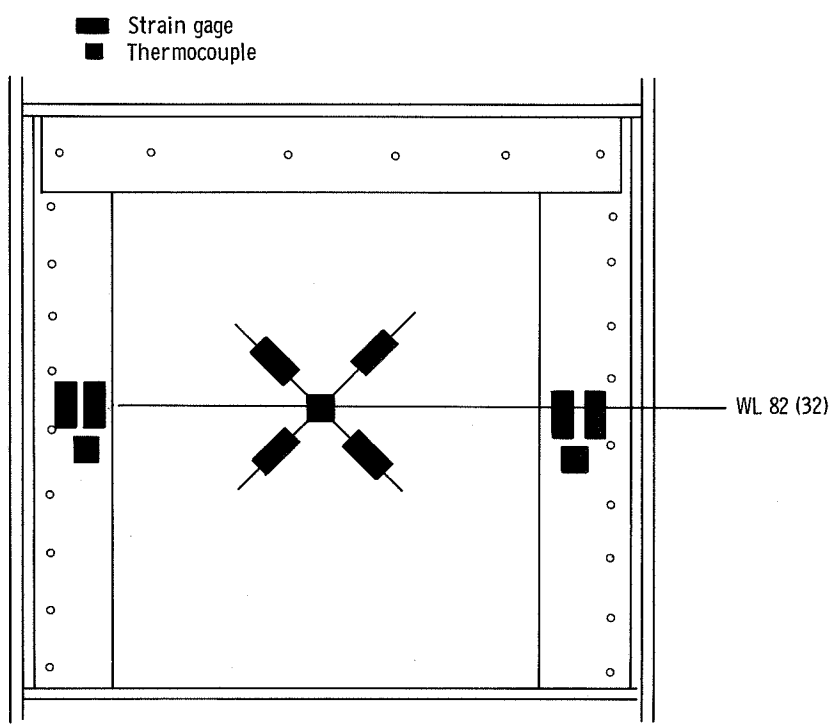

(d) Rear spar, views C-C and D-D.

Figure 5. Concluded.

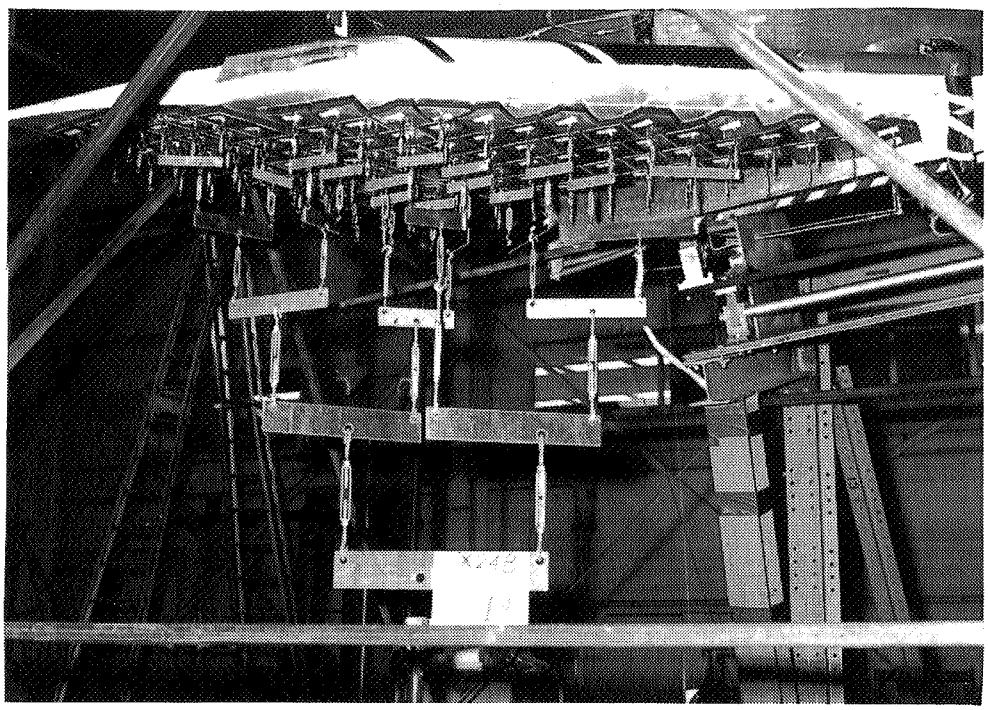

Figure 6. Fin in calibration loading fixture.

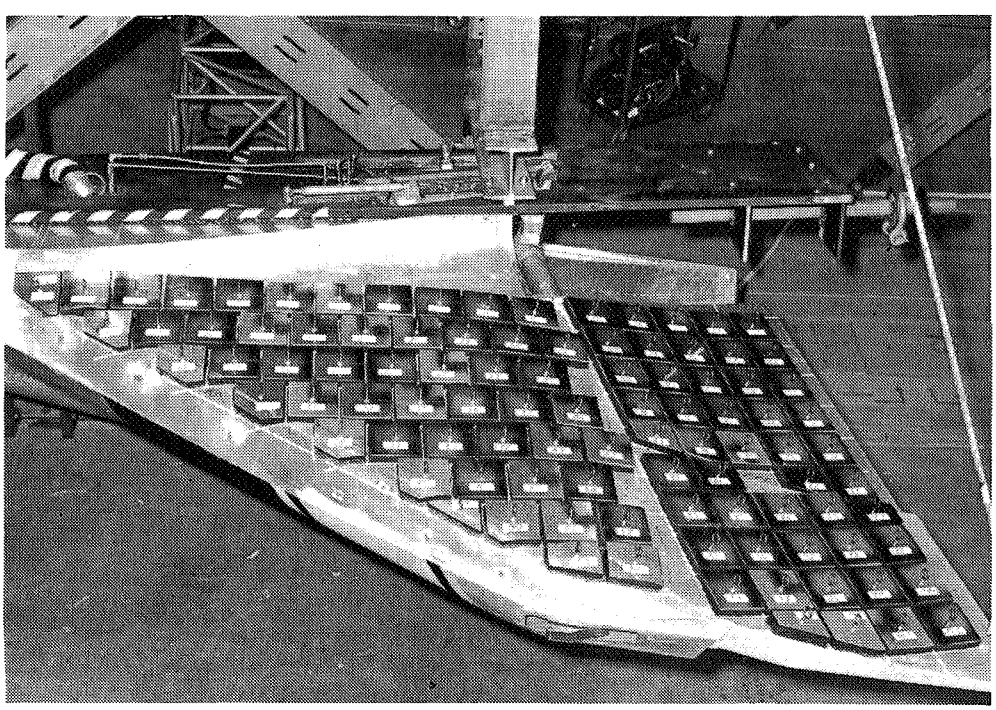

Figure 7. Fin and load pads.

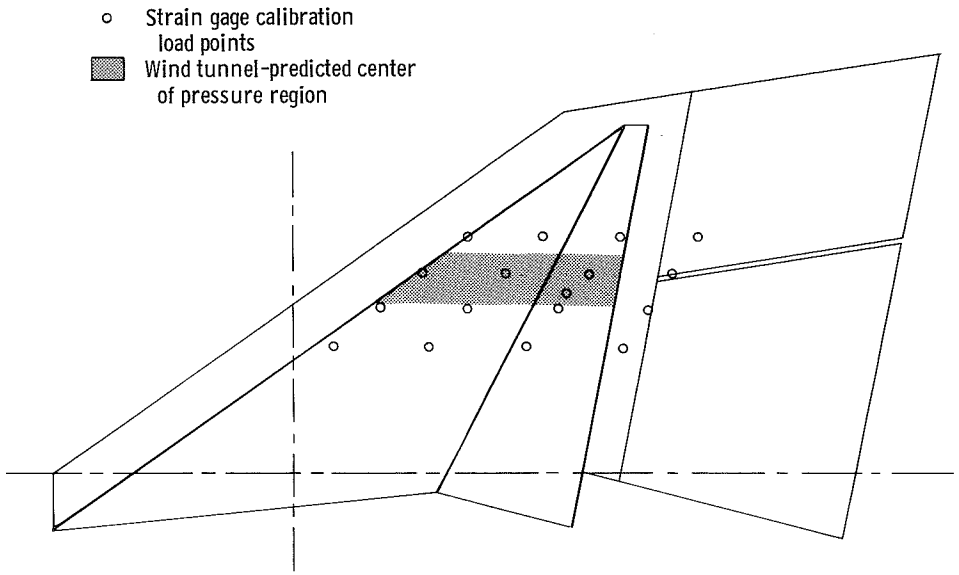

Figure 8. Strain gage calibration load points and wind tunnel-predicted center of pressure region.

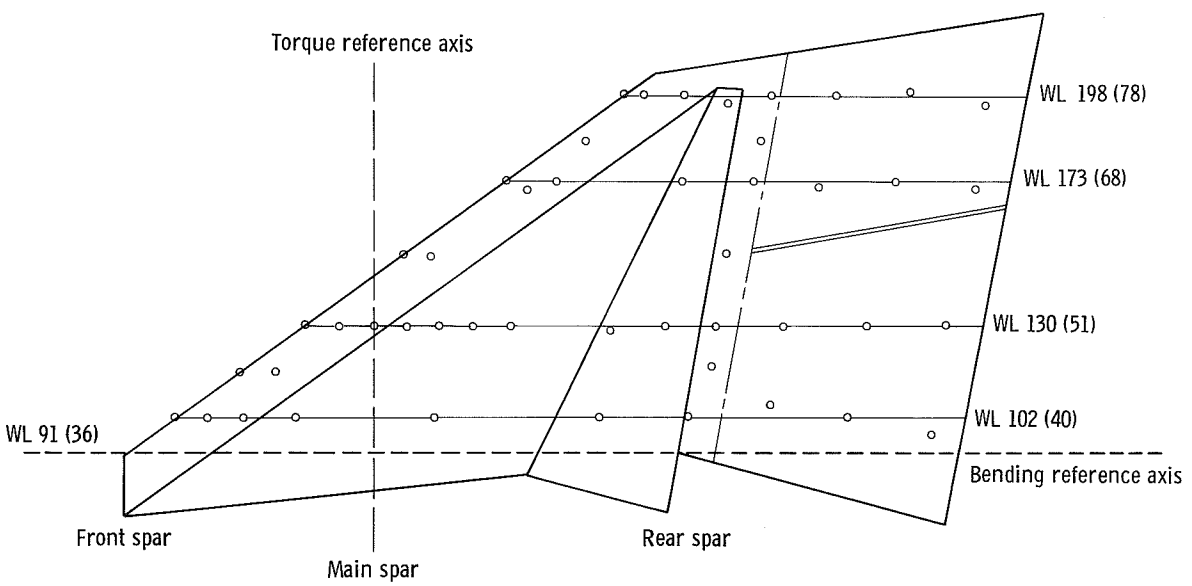

(a) Taps on left fin and left upper and lower rudders. Except for leading edge orifices, all orifices are on both sides of fin and rudders. Dimensions in centimeters (inches).

Figure 9. Pressure tap locations.

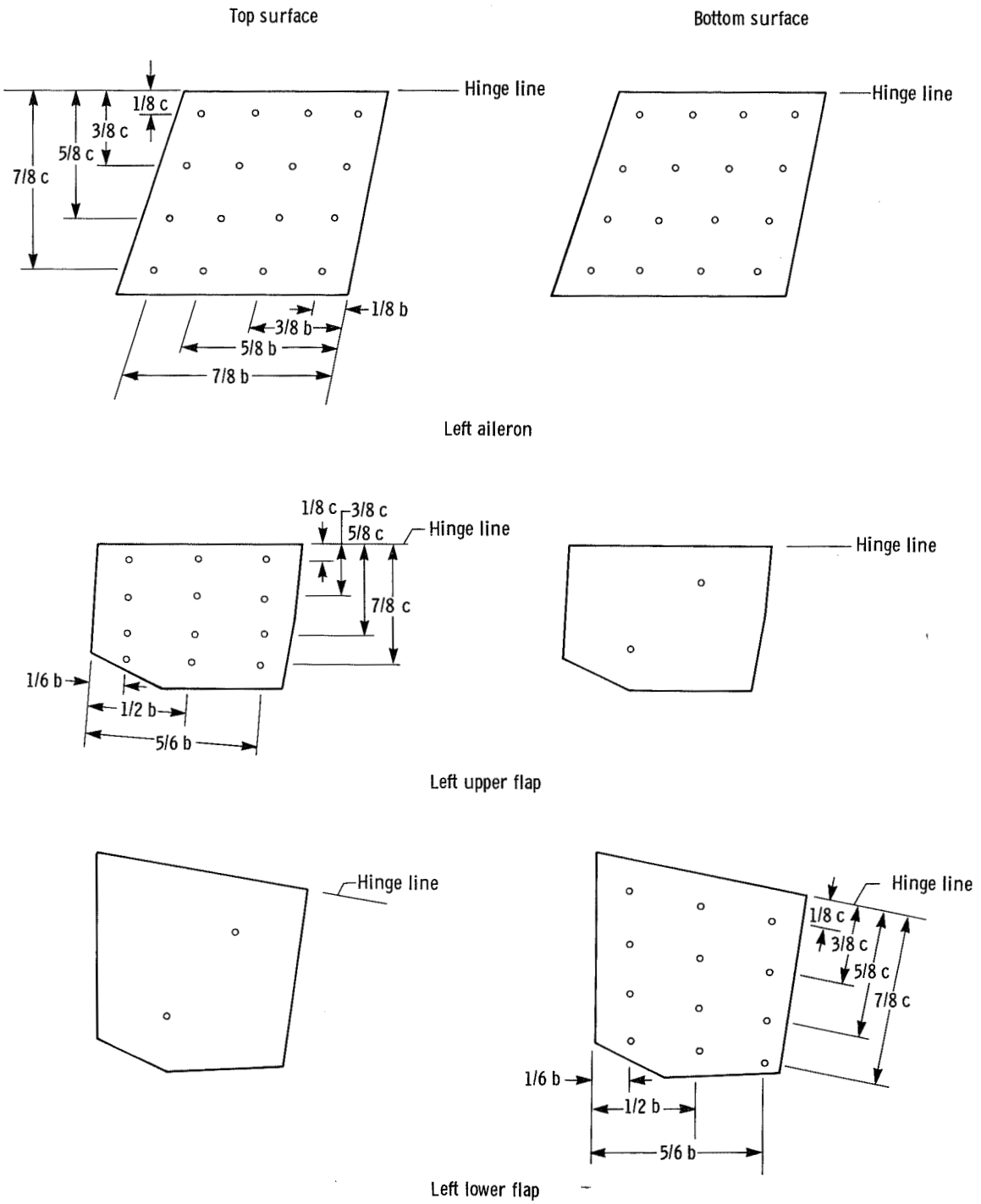

(b) Taps on left aileron and left upper and lower flaps.

Figure 9. Concluded.

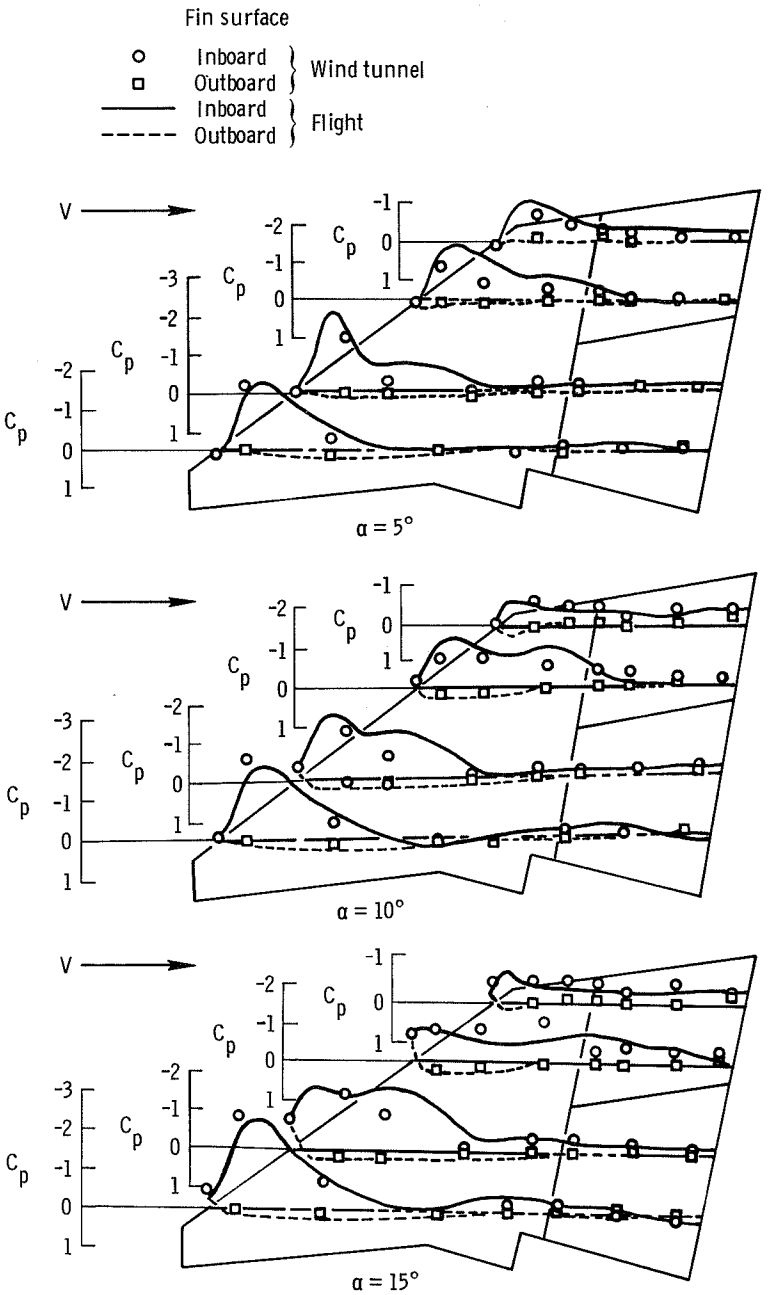

(a) M = 0.6.

Figure 10. Comparison of flight-measured and wind tunnel-predicted left fin pressure distributions. $\beta = 0°$; $\delta_{rb} = 0°$; $\delta_{ab} = 7°$; $\delta_{ub} = -40°$.

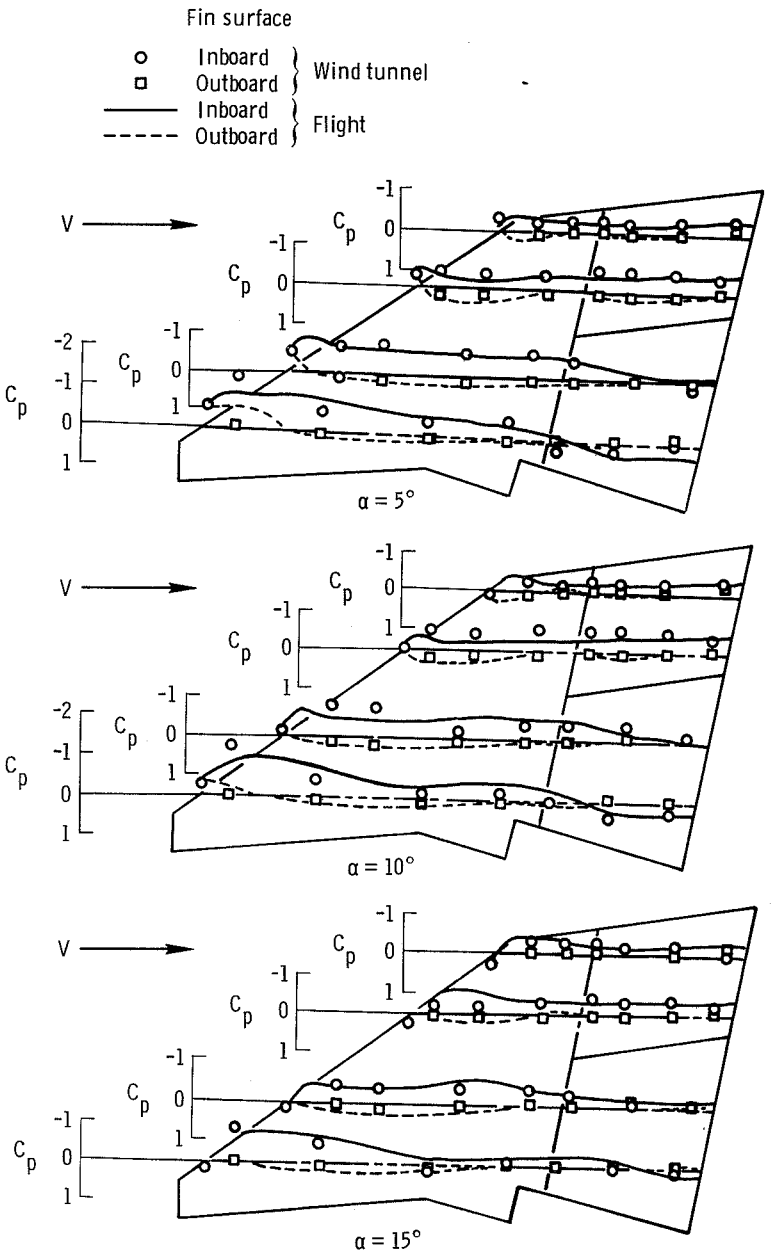

(b) M = 0.9.

Figure 10. Continued.

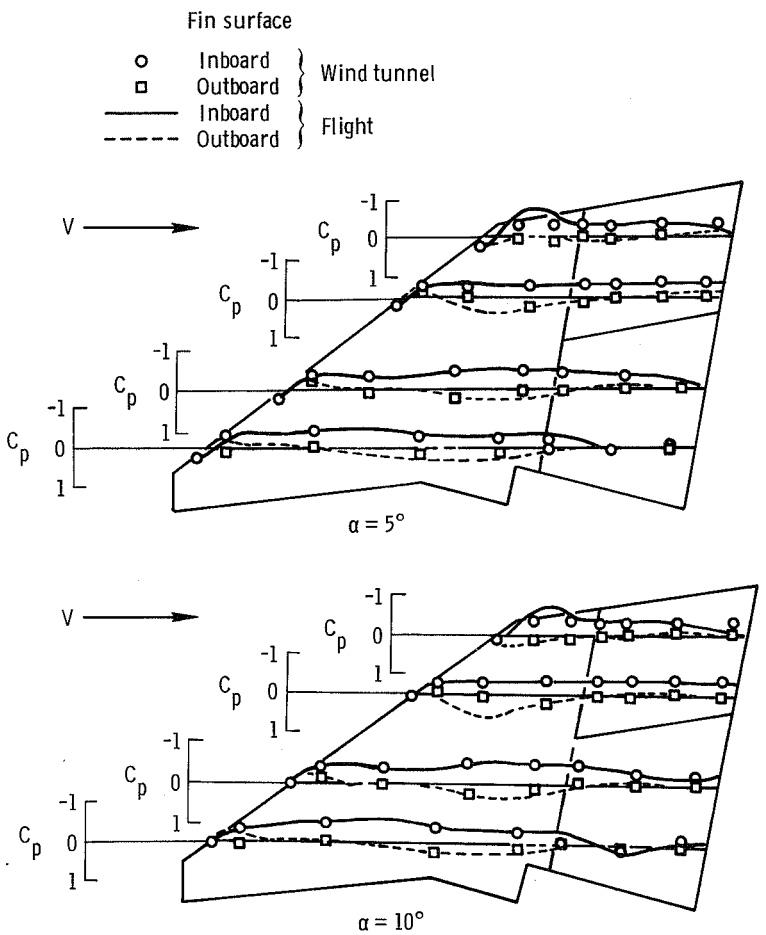

(c) Flight, M = 1.2; wind tunnel, M = 1.3.

Figure 10. Concluded.

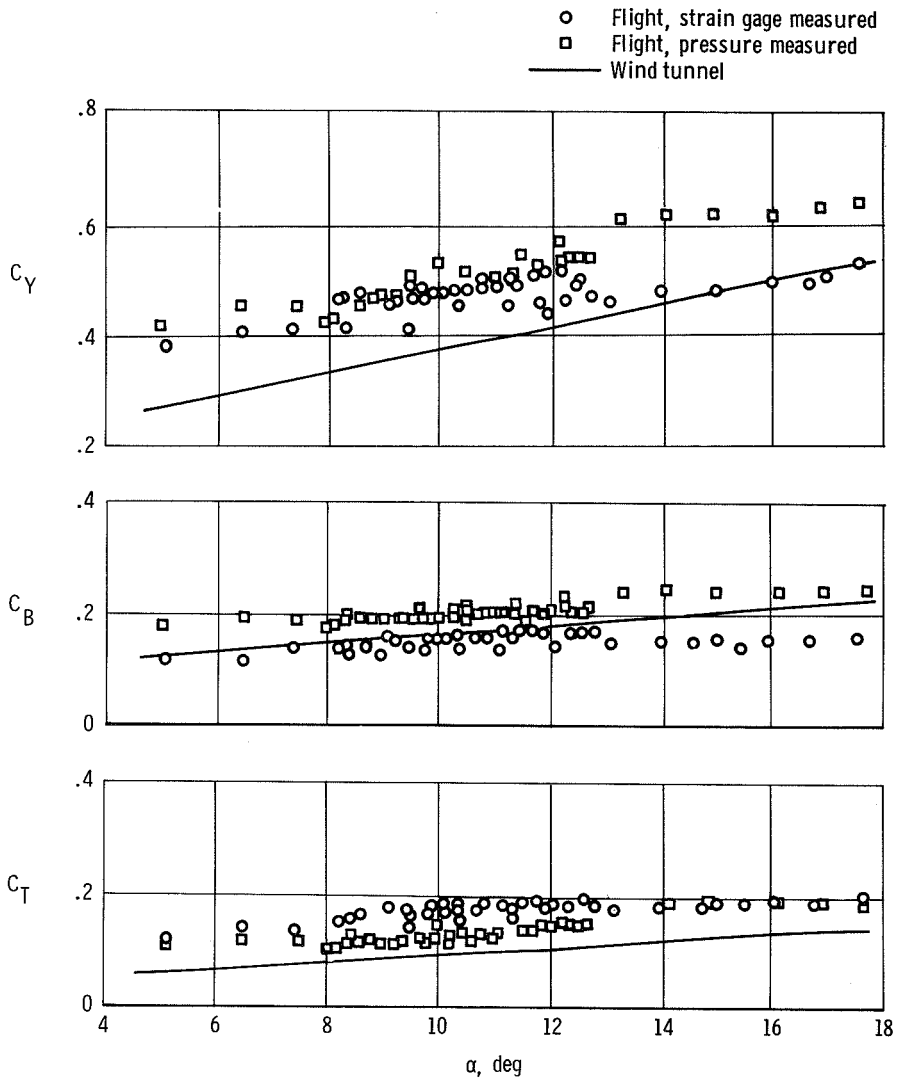

(a) M = 0.6.

Figure 11. Variation of left fin normal-force, bending-moment, and torque coefficients with angle of attack. $\beta = 0°$; $\delta_{rb} = 0°$; $\delta_{ab} = 7°$; $\delta_{ub} = -40°$; *flight,* $\delta_l = 15°$ *to* $25°$; *wind tunnel,* $\delta_l = 20°$.

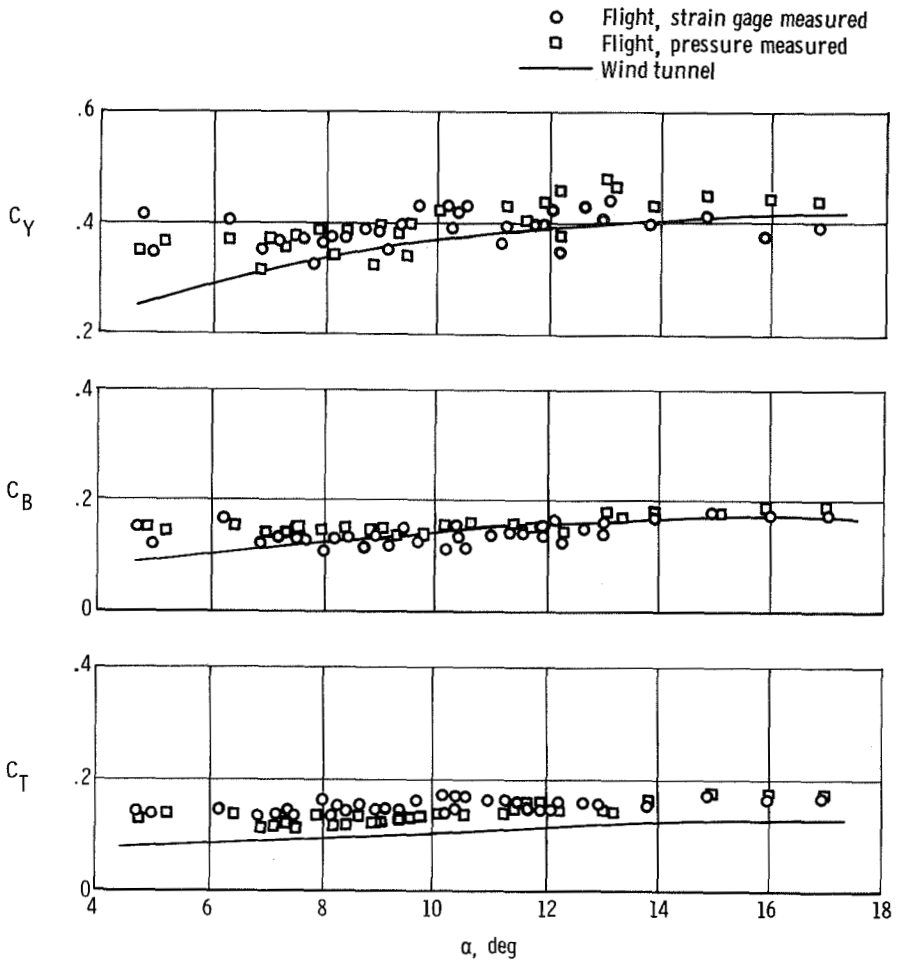

(b) $M = 0.9$.

Figure 11. Continued.

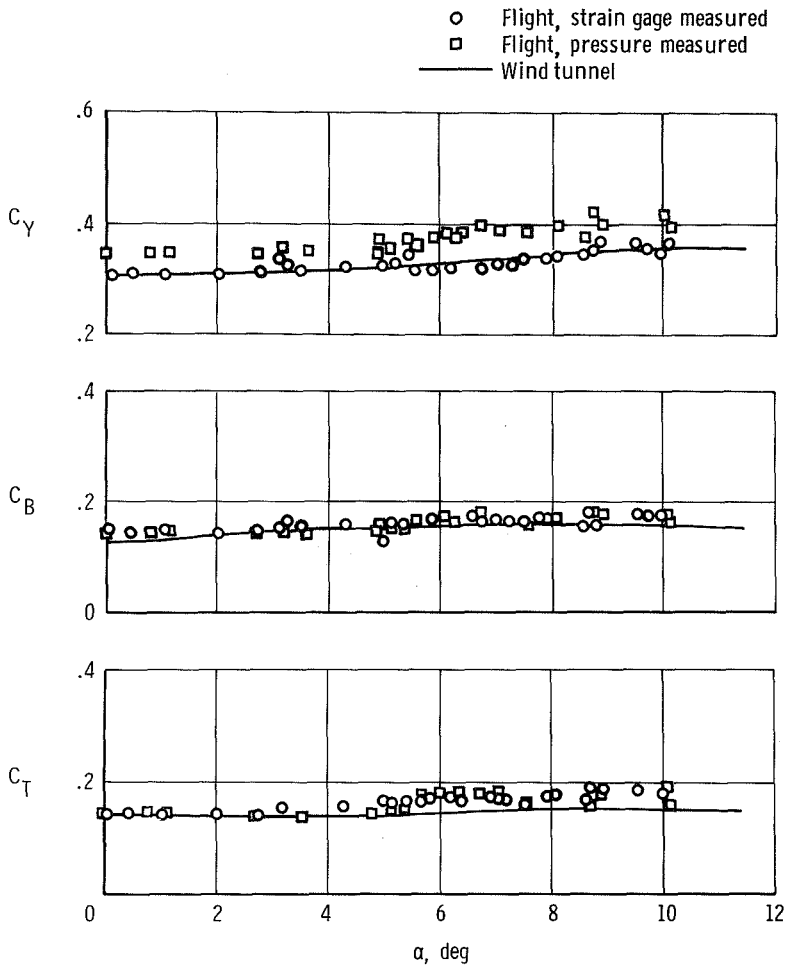

(c) Flight, M = 1.2; wind tunnel, M = 1.3.

Figure 11. Concluded.

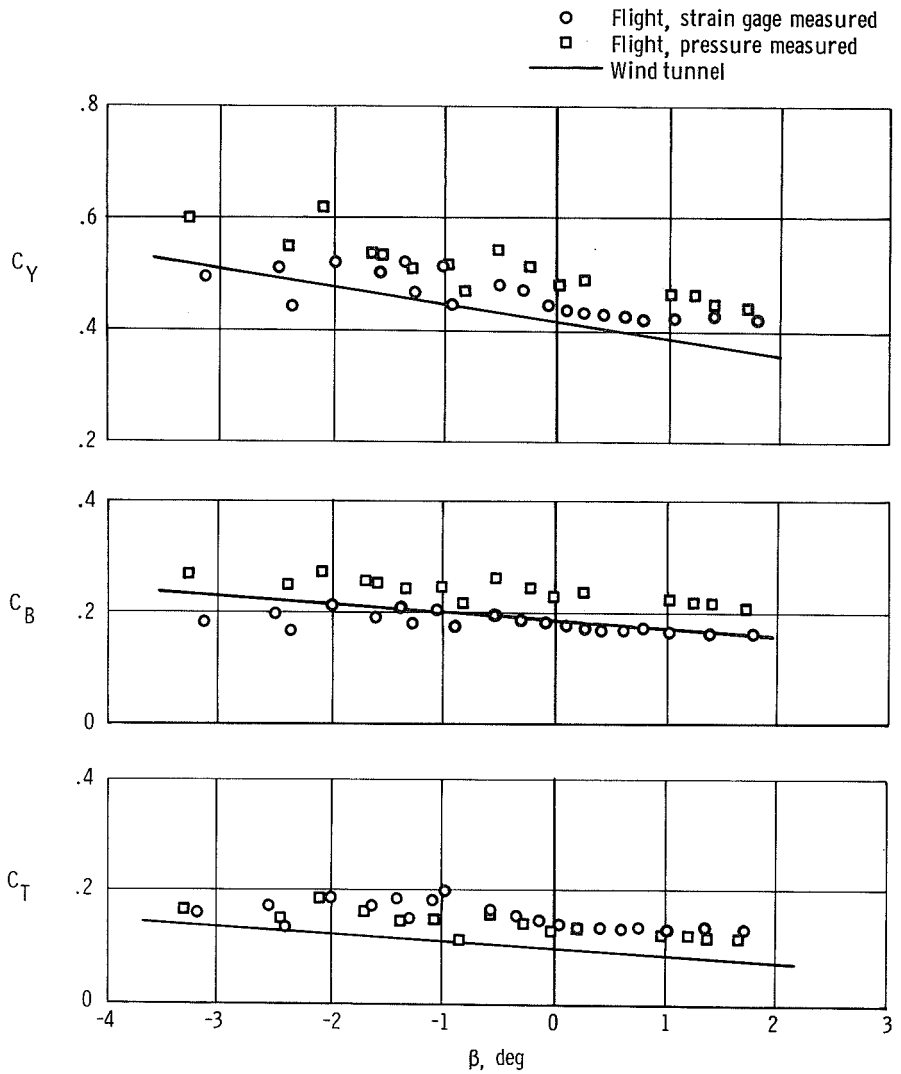

(a) $M = 0.6$, $\alpha = 12°$.

Figure 12. Variation of left fin normal-force, bending-moment, and torque coefficients with angle of sideslip. $\delta_{rb} = 0°$; $\delta_{ab} = 7°$; $\delta_{ub} = -40°$; *flight,* $\delta_l = 12°$; *wind tunnel,* $\delta_l = 20°$.

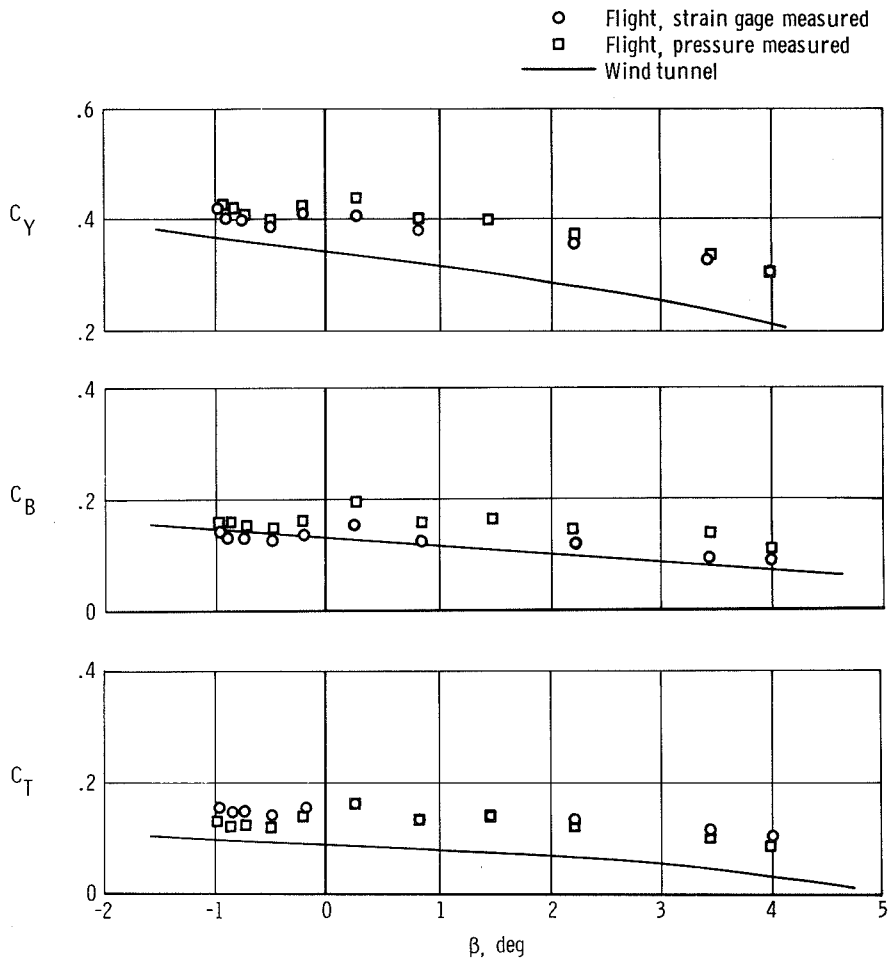

(b) $M = 0.9$, $\alpha = 8°$.

Figure 12. Continued.

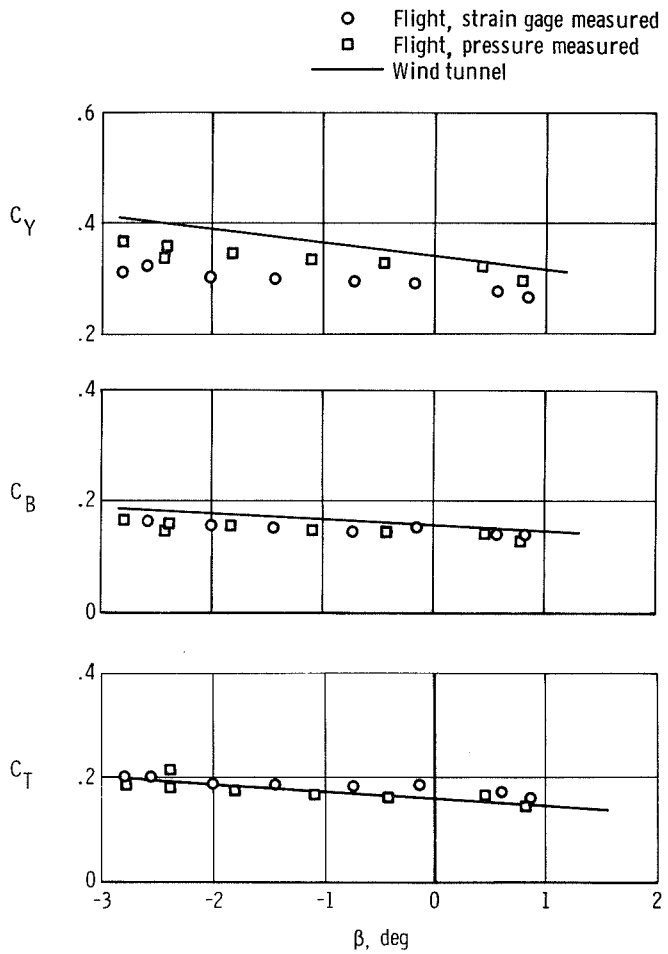

(c) Flight, M = 1.4, α = 8°; wind tunnel, M = 1.3, α = 8°.

Figure 12. Concluded.

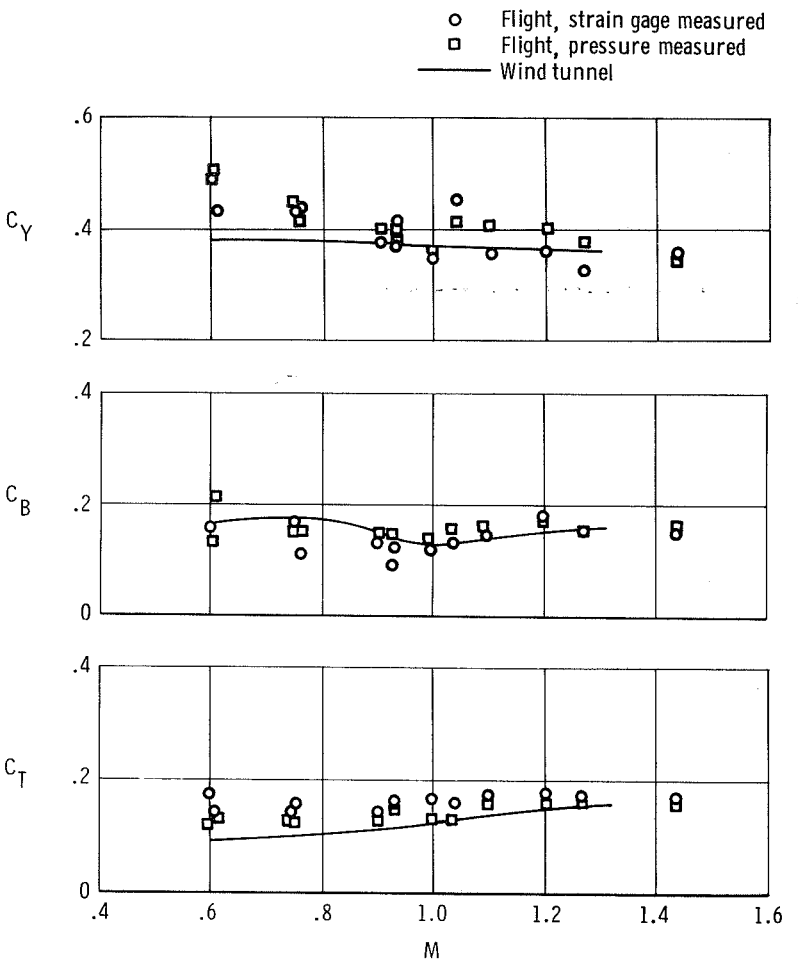

Figure 13. Variation of left fin normal-force, bending-moment, and torque coefficients with Mach number. $\alpha = 10°$; $\beta = 0°$; $\delta_{rb} = 0°$; $\delta_{ab} = 7°$; $\delta_{ub} = -40°$; *flight,* $\delta_l = 15°$ *to* $25°$; *wind tunnel,* $\delta_l = 20°$.

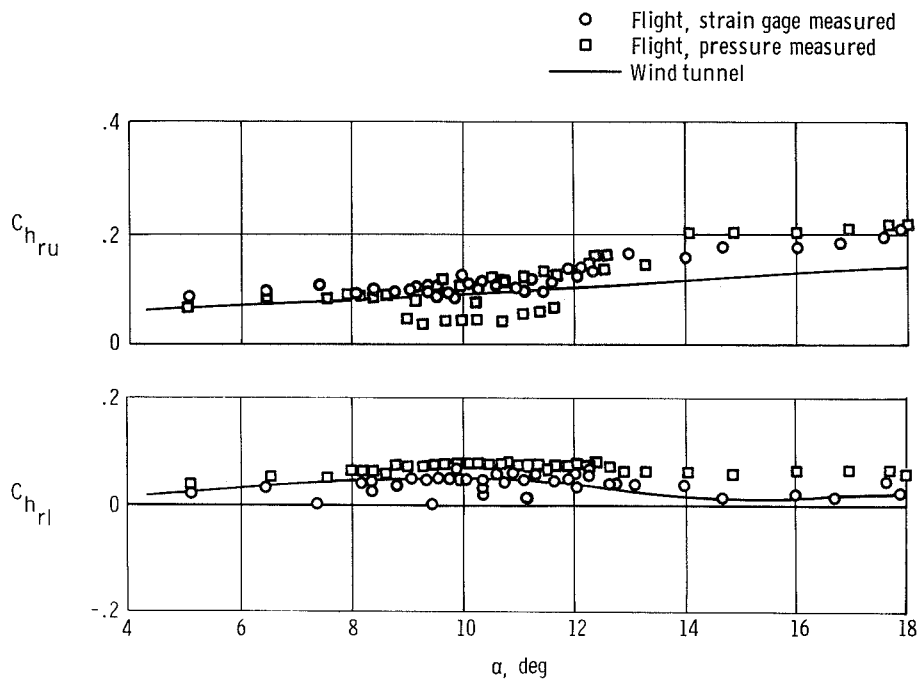

(a) M = 0.6.

Figure 14. Variation of upper and lower rudder hinge-moment coefficients with angle of attack. $\beta = 0°$; $\delta_{rb} = 0°$; $\delta_{ab} = 7°$; $\delta_{ub} = -40°$; *flight,* $\delta_l = 15°$ *to* $25°$; *wind tunnel,* $\delta_l = 20°$.

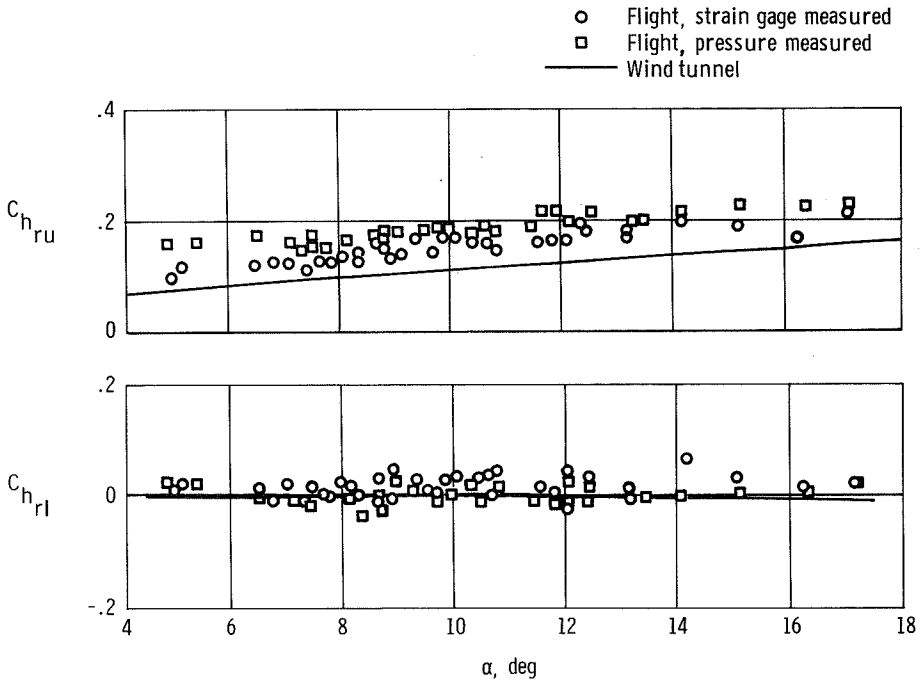

(b) M = 0.9.

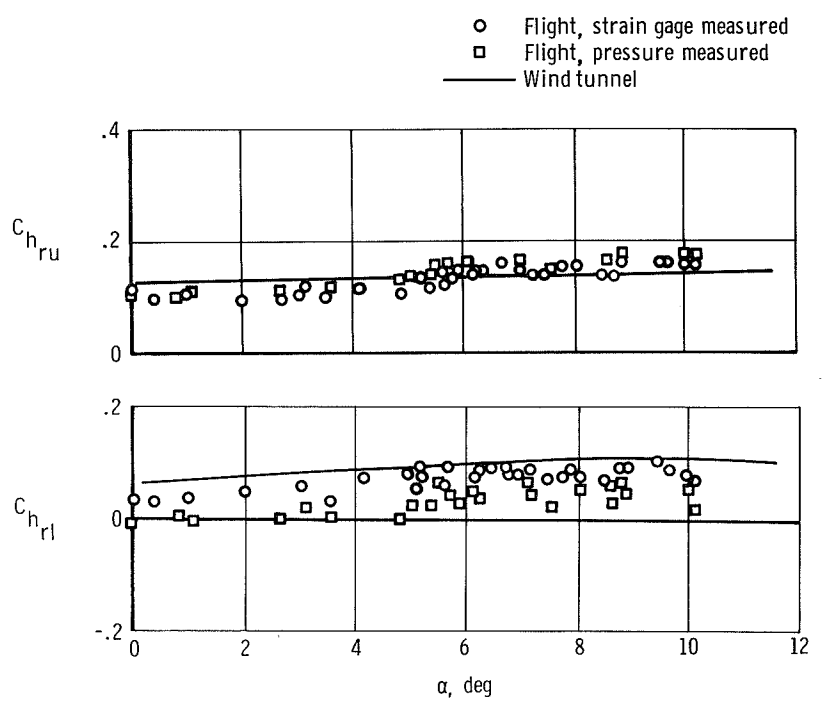

(c) Flight, M = 1.2; wind tunnel, M = 1.3.

Figure 14. Concluded.

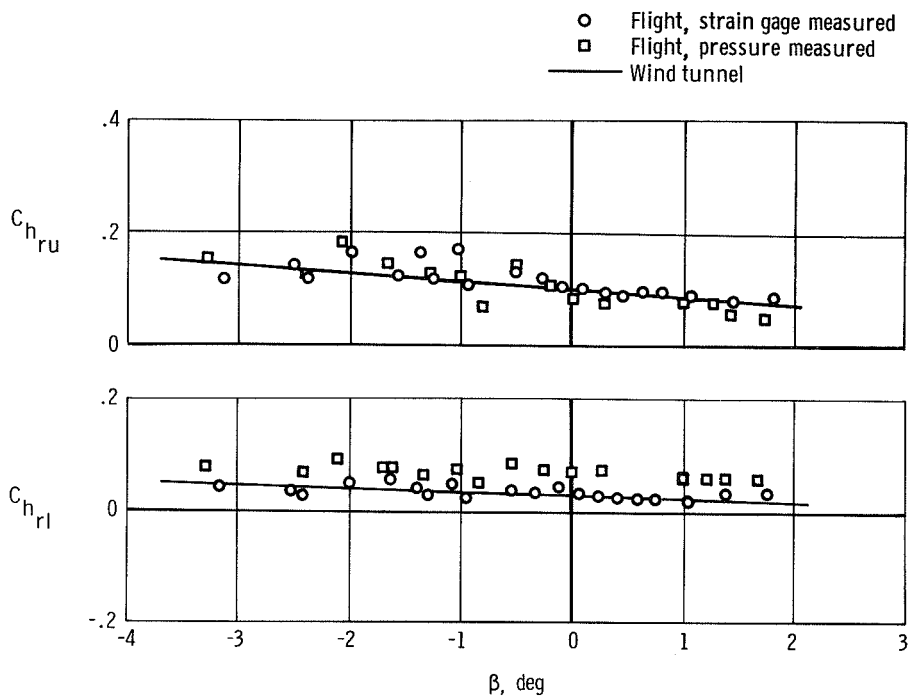

(a) $M = 0.6$, $\alpha = 12°$.

Figure 15. Variation of upper and lower rudder hinge-moment coefficients with angle of sideslip. $\delta_{rb} = 0°$; $\delta_{ab} = 7°$; $\delta_{ub} = -40°$; flight, $\delta_l = 15°$ to $25°$; wind tunnel, $\delta_l = 20°$.

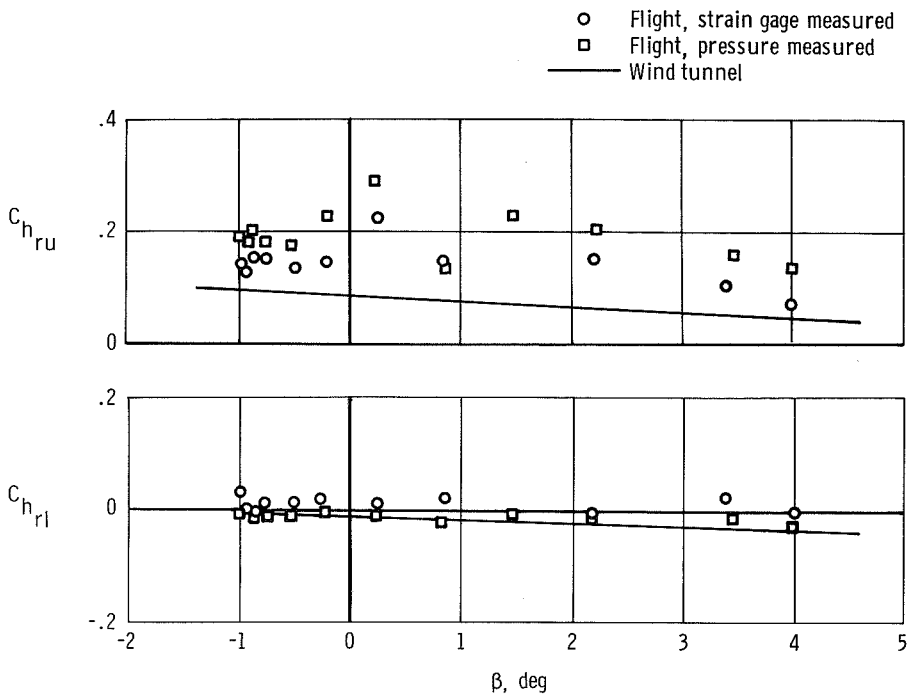

(b) $M = 0.9$, $\alpha = 8°$.

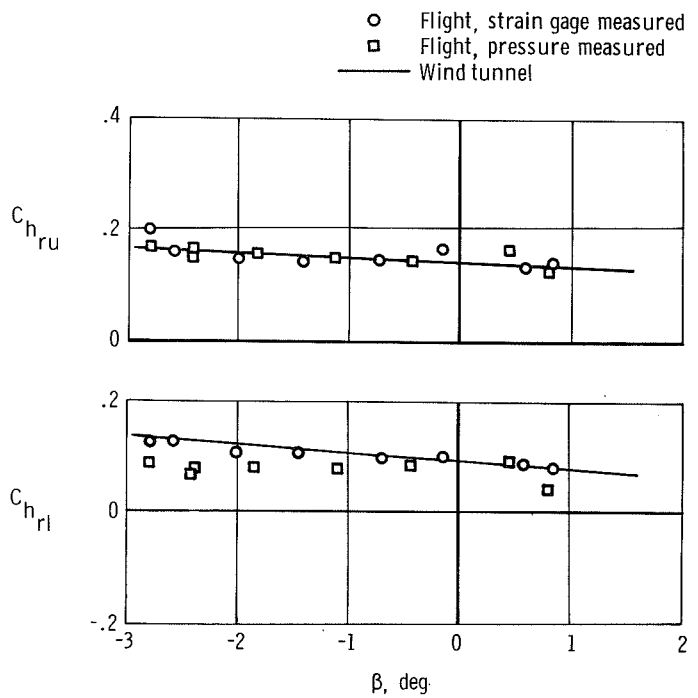

(c) Flight, $M = 1.4$, $\alpha = 8°$; wind tunnel, $M = 1.3$, $\alpha = 8°$.

Figure 15. Concluded.

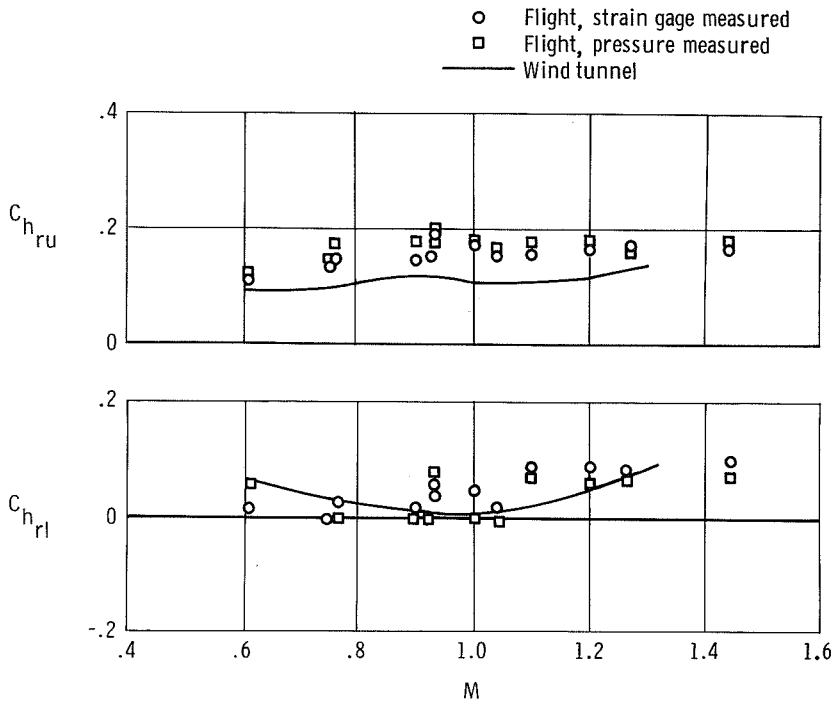

Figure 16. Variation of upper and lower rudder hinge-moment coefficients with Mach number. $\alpha = 10°$; $\beta = 0°$; $\delta_{rb} = 0°$; $\delta_{ab} = 7°$; $\delta_{ub} = -40°$; *flight,* $\delta_l = 15°$ *to* $25°$; *wind tunnel,* $\delta_l = 20°$.

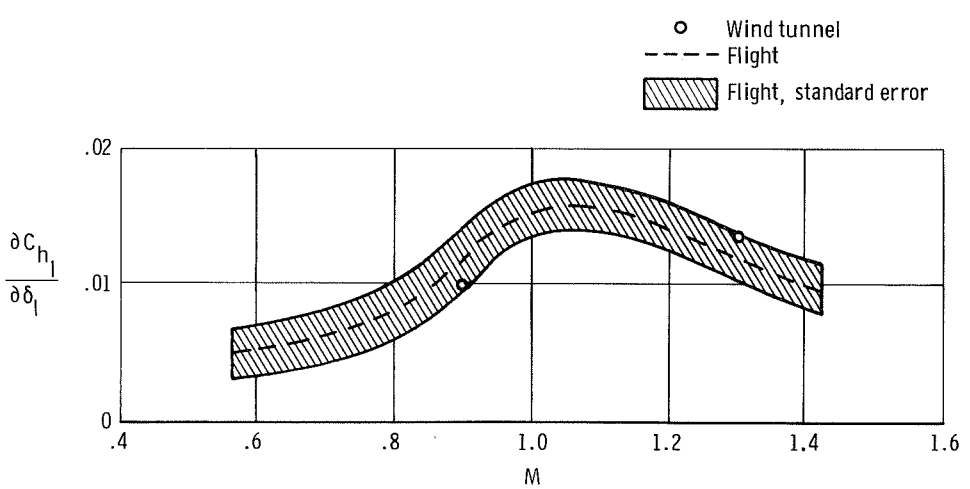

Figure 17. Variation of the lower flap hinge-moment coefficient due to lower flap deflection with Mach number. $\delta_{rb} = 0°$; $\delta_{ab} = 7°$; $\delta_{ub} = -40°$.

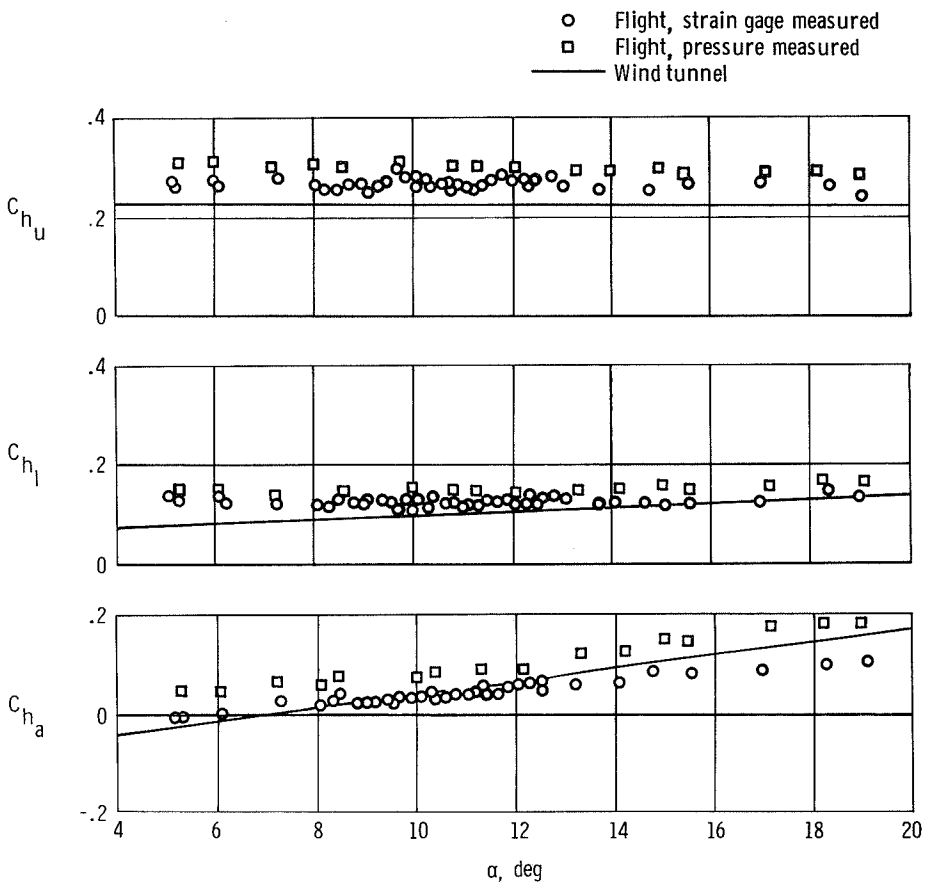

(a) M = 0.6.

Figure 18. Variation of upper flap, lower flap, and aileron hinge-moment coefficients with angle of attack. $\beta = 0°$; $\delta_{rb} = 0°$; $\delta_{ab} = 7°$; $\delta_{ub} = -40°$; $\delta_l = 20°$ *(flight,* C_{h_l} *corrected to* $\delta_l = 20°$*).*

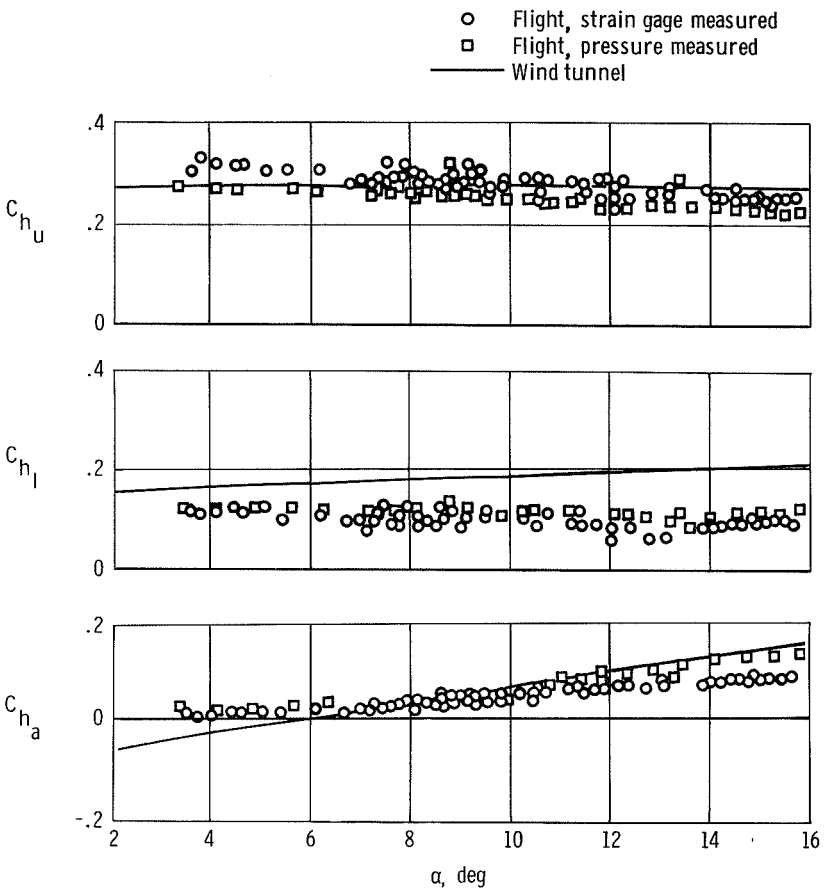

(b) M = 0.9.

Figure 18. Continued.

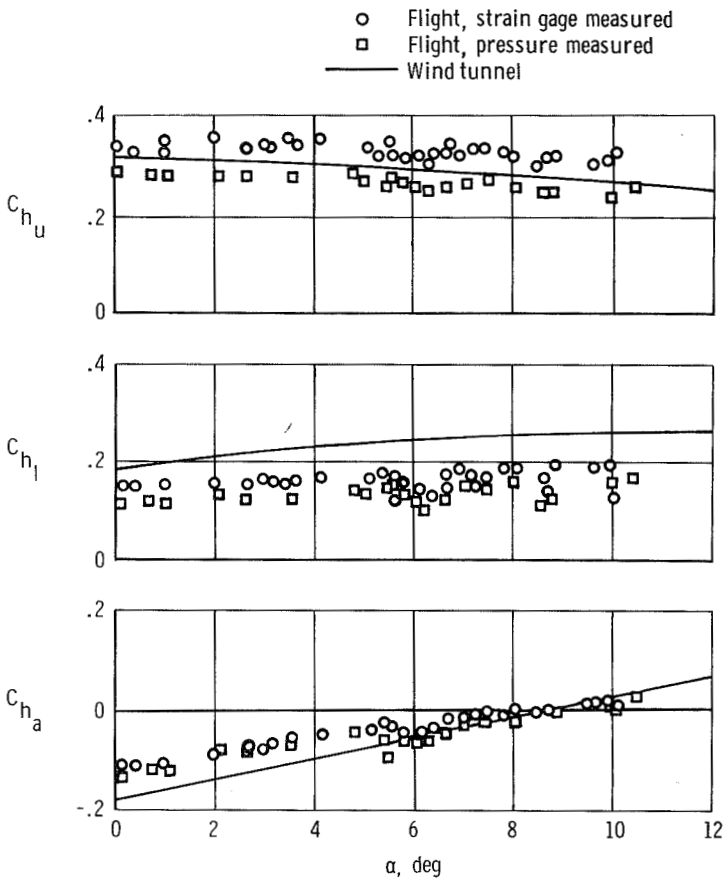

(c) Flight, M = 1.2; wind tunnel, M = 1.3.

Figure 18. Concluded.

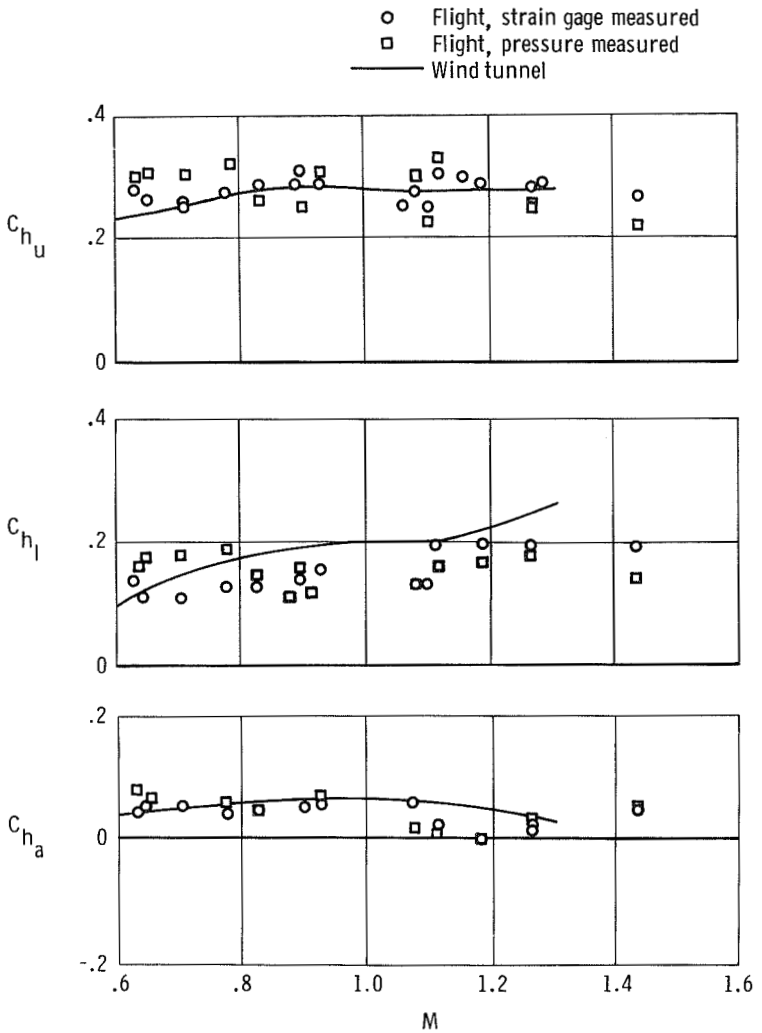

Figure 19. Variation of upper flap, lower flap, and aileron hinge-moment coefficients with Mach number. $\alpha = 10°$; $\beta = 0°$; $\delta_{rb} = 0°$; $\delta_{ab} = 7°$; $\delta_u = -40°$; $\delta_l = 20°$ *(flight,* C_{h_l} *corrected to* $\delta_l = 20°$*).*

1. Report No.	2. Government Accession No.	3. Recipient's Catalog No.
NASA TP-1331		

4. Title and Subtitle	5. Report Date
COMPARISON OF CONCURRENT STRAIN GAGE- AND PRESSURE TRANSDUCER-MEASURED FLIGHT LOADS ON A LIFTING REENTRY VEHICLE AND CORRELATION WITH WIND TUNNEL PREDICTIONS	October 1978
	6. Performing Organization Code H-1035

7. Author(s)	8. Performing Organization Report No.
Ming H. Tang, Walter J. Sefic, and Robert G. Sheldon	
	10. Work Unit No. 521-71-01
9. Performing Organization Name and Address	
NASA Dryden Flight Research Center P.O. Box 273 Edwards, California 93523	11. Contract or Grant No.
	13. Type of Report and Period Covered Technical Paper
12. Sponsoring Agency Name and Address	
National Aeronautics and Space Administration Washington, D.C. 20546	14. Sponsoring Agency Code

15. Supplementary Notes

Much of the information presented herein was previously made available to U.S. Government Agencies in NASA TM X-56042.

16. Abstract

Concurrent strain gage- and pressure transducer-measured flight loads on a lifting reentry vehicle are compared and correlated with wind tunnel-predicted loads. Subsonic, transonic, and supersonic aerodynamic loads are presented for the left fin and control surfaces of the X-24B lifting reentry vehicle. Typical left fin pressure distributions are shown. The effects of variations in angle of attack, angle of sideslip, and Mach number on the left fin loads and rudder hinge moments are presented in coefficient form. Also presented are the effects of variations in angle of attack and Mach number on the upper flap, lower flap, and aileron hinge-moment coefficients. The effects of variations in lower flap hinge moments due to changes in lower flap deflection and Mach number are presented in terms of coefficient slopes.

17. Key Words (Suggested by Author(s))	18. Distribution Statement
X-24B lifting reentry vehicle Flight loads Wind tunnel loads Concurrent strain gage and pressure measurements	Unclassified—Unlimited Category: 02

19. Security Classif. (of this report)	20. Security Classif. (of this page)	21. No. of Pages	22. Price*
Unclassified	Unclassified	43	$3.75

*For sale by the National Technical Information Service, Springfield, Virginia 22161

NASA-Langley, 1978

National Aeronautics and Space Administration

Washington, D.C.
20546

Official Business
Penalty for Private Use, $300

THIRD-CLASS BULK RATE

Postage and Fees Paid
National Aeronautics and
Space Administration
NASA-451

NASA

POSTMASTER: If Undeliverable (Section 158 Postal Manual) Do Not Return